

University of Nebraska - Lincoln

DigitalCommons@University of Nebraska - Lincoln

Mechanical & Materials Engineering Faculty
Publications

Mechanical & Materials Engineering, Department
of

2017

Rapidly Solidified Rare-Earth Permanent Magnets: Processing, Properties, and Applications

Shampa Aich

Indian Institute of Technology Kharagpur, saich@metal.iitkgp.ernet.in

Dillip K. Satapathy

Indian Institute of Technology Madras, dks@iitm.ac.in

Jeffrey E. Shield

University of Nebraska-Lincoln, jshield@unl.edu

Follow this and additional works at: <http://digitalcommons.unl.edu/mechengfacpub>



Part of the [Mechanics of Materials Commons](#), [Nanoscience and Nanotechnology Commons](#), [Other Engineering Science and Materials Commons](#), and the [Other Mechanical Engineering Commons](#)

Aich, Shampa; Satapathy, Dillip K.; and Shield, Jeffrey E., "Rapidly Solidified Rare-Earth Permanent Magnets: Processing, Properties, and Applications" (2017). *Mechanical & Materials Engineering Faculty Publications*. 352.

<http://digitalcommons.unl.edu/mechengfacpub/352>

This Article is brought to you for free and open access by the Mechanical & Materials Engineering, Department of at DigitalCommons@University of Nebraska - Lincoln. It has been accepted for inclusion in Mechanical & Materials Engineering Faculty Publications by an authorized administrator of DigitalCommons@University of Nebraska - Lincoln.

Published in *Advances in Magnetic Materials: Processing, Properties, and Performance*,
 1st Edition, ed. Sam Zhang & Dongliang Zhao. CRC Press.
 Copyright 2017 Taylor & Francis Group. Used by permission.
 Published February 16, 2017.

Rapidly Solidified Rare-Earth Permanent Magnets: *Processing, Properties, and Applications*

Shampa Aich,¹ Dillip K. Satapathy,² and J. E. Shield³

1 Indian Institute of Technology Kharagpur, saich@metal.iitkgp.ernet.in

2 Indian Institute of Technology Madras, dks@iitm.ac.in

3 University of Nebraska–Lincoln, jshield@unl.edu

Contents

| | |
|--|----|
| Abstract | 2 |
| 1 Introduction | 2 |
| 2 Various Processing Routes for Rare-Earth Permanent Magnets | 8 |
| 2.1 Powder Metallurgy Route | 8 |
| 2.2 Hydrogen-Assisted Processing | 10 |
| 2.2.1 Hydrogenation–Disproportionation–Desorption–Recombination | 10 |
| 2.2.2 Reactive Milling in Hydrogen | 11 |
| 2.3 Mechanical Alloying | 13 |
| 2.4 Rapid Solidification Techniques | 14 |
| 2.4.1 Atomization | 15 |
| 2.4.2 Surface Melting by Laser and Resolidification | 17 |
| 2.4.3 Electrospinning | 21 |
| 2.4.4 Melt Spinning | 21 |
| 2.4.5 Melt Extraction | 24 |
| 3 Rapidly Solidified Rare-Earth Permanent Magnets | 25 |
| 3.1 RCo/Sm–Co-Based Magnets | 26 |
| 3.1.1 Addition of Alloying Elements/Stabilizing (1:7) Phase | 27 |
| 3.1.2 Addition of C/B as a Grain Refiner | 31 |

| | |
|---|----|
| 3.1.3 Effect of Wheel Speed and Heat Treatment | 35 |
| 3.1.4 Rare-Earth Magnets as High-Temperature Magnets | 36 |
| 3.1.5 Oxidation Protection for Sm–Co Magnets | 37 |
| 3.2 R–Fe–B-Based Magnets/Nd–Fe–B-Based Magnets | 38 |
| 3.2.1 Sintered Magnets | 39 |
| 3.2.2 Bonded Magnets | 39 |
| 3.2.3 Nanocrystalline Permanent Magnets | 42 |
| 3.2.4 Nanocomposite Magnets | 44 |
| 3.2.5 Protective Coating to Improve Corrosion Resistance | 44 |
| 3.3 Interstitially Modified R_2Fe_{17} -Based Permanent Magnets | 45 |
| 3.4 New Materials/Nanocomposites/Thin-Film Magnets | 52 |
| 4 Applications of Rare-Earth Permanent Magnets | 53 |
| 5 Conclusions and Future Perspectives | 56 |
| Acknowledgments | 56 |
| References | 57 |

Abstract

Rapidly solidified rare-earth-based permanent magnets are considered to have better potential as permanent magnets compared to the conventional bulk materials, which can be attributed to their improved microstructure and better magnetic properties compared to rare-earth magnets synthesized by the conventional (powder metallurgy) routes. The performance (quality) of these magnets depends on the thermodynamics and kinetics of the different processing routes, such as atomization, melt spinning, and melt extraction. Here, we review the various processing routes of rapidly solidified rare-earth permanent magnets and the related properties and applications. In the review, some specific alloy systems, such as Sm–Co-based alloys, Nd–Fe–B, and interstitially modified Fe-rich rare-earth magnets are discussed in detail mentioning their processing routes and subsequently achieved crystal structure, microstructure and magnetic properties, and the related scopes for various applications. Some newly developed nanocomposites and thin-film magnets are also included in the discussion.

1 Introduction

Rare-earth permanent magnets have revolutionized technology since their discovery in the 1970s and are ubiquitous in this information-technology-driven and energy-conscious world. Rare-earth magnets have allowed the miniaturization of countless devices and the development of highly efficient motors and generators. These magnets are stronger than the conventional magnets of ferrites or Alnico. Since the discovery of the naturally occurring mineral, magnetite (Fe_3O_4), magnetism and magnetic materials have been playing an important role in modern science and technology. In ancient times, the Chinese and the Greeks were using lodestones or “waystones” in guiding mariners. In 1600, physicist William Gilbert experimented

with lodestone, iron magnets, and the magnetic field of the earth. His experiments laid the foundation for current scientific applications and dispelled the folklore surrounding magnetism and magnetic material [1]. Research about magnetic materials expanded after the invention of electromagnets by physicist Hans Christian Oersted in 1820 [1]. Permanent magnets have brought much more attention to the field, because unlike powerful electromagnets, they can be used without any consumption of electricity or generation of heat.

Permanent magnets are used and extensively studied in academic and military research and energy laboratories. Another important area of application is in medical industries (MRI, hematology laboratories, and magnetic hyperthermia technique). About 160 magnets are used for different purposes in our daily lives. The applications range from refrigerator magnets, kitchen appliances, television, telephone, watches, computer, and audio systems to microelectronics. Another 100 magnets are used in the automobile industry. Permanent magnets are behind some of the most important inventions of our modern lives. They make our lives pleasant, comfortable, and easier. They have a promising future, because a number of new devices are waiting for them. Ultimately, there is a basic necessity to understand and improve their properties, as well as to look for new applications for them.

The first commonly used permanent magnets were made of carbon steel and were shaped like a horseshoe. Although this type of magnet is now obsolete, the horseshoe represents the symbol for magnetism [2]. In the past 60 years, the applications of permanent magnets have been diversified due to discoveries of new materials such as Alnicos (alloys of Al, Ni, Co, and Fe), ferrites (combination of iron oxide with another metal), Nd-Fe-B, and Sm-Co magnets. Although the Alnicos were extensively used in the mid-twentieth century as general-purpose permanent magnets, for their moderate magnetic properties achieved by relatively easy processing, they were replaced by much cheaper ferrites, which now occupy 55% of the permanent magnet world market.

The dawn of rare-earth permanent magnets was the discovery of the high anisotropy field of SmCo_5 in the late 1960s [3,4]. People were much more attentive to these Sm-Co magnets due to their high anisotropy field H_A , which was twice that of contemporary ferromagnetic Alnico alloys. Magnets made from rare-earth materials exhibit magnetic fields up to 1.4 T whereas ferrites and Alnico magnets exhibit magnetic fields in the range of 0.4–1 T. Since rare-earth magnets are extremely brittle and vulnerable to corrosive environment, they are coated with other materials to improve their corrosion resistance. Rare-earth elements are mostly alloyed with Co, Fe, and Ni since in pure form these elements have Curie temperatures below room temperature. This also leads to an increase in the magnetic anisotropy of the alloy. The high magnetic anisotropy of rare-earth magnets can be attributed to

the unfilled f shells, which can contain up to seven unpaired electrons (as in gadolinium) with aligned electron spin. This anisotropy makes these alloys easy to magnetize in one direction while hard to magnetize in the other direction. These unpaired electrons behave as local paramagnets as they easily retain their magnetic moments. A higher anisotropy field increases the coercivity H_{ci} , which helps to increase the maximum energy product $(BH)_{max}$, the amount of energy stored inside the material. When forming compounds with magnetic transition metals Fe, Co, and Ni, the spin-orbit coupling results in extremely high magnetic anisotropy, which coupled with the relatively high magnetization of Fe, Co, and Ni results in the necessary recipe for high-energy densities. The important parameters that characterize the performance of a permanent magnet are as follows:

- High saturation magnetization M_s
- High remanence M_r
- Very high uniaxial magnetocrystalline anisotropy energy K_1 : high coercivity H_c
- High maximum energy product $(BH)_{max}$
- High Curie temperature T_c

The other important factors are good temperature stability, mechanical strength, machinability, and low cost. A typical hysteresis curve (magnetization M vs. field H) for a permanent magnet has been shown in **Figure 1** mentioning the important parameters discussed earlier. Another version of hysteresis curve is also available where the ordinate shows the magnetic induction (B) instead of the magnetization (M), and the curve is magnetic induction B versus field H type curve. Among all the aforementioned factors, the most important one is the maximum energy product $(BH)_{max}$ as this is the most representative quantity of a permanent magnet. The maximum energy product is the maximum value of the product of the magnetic induction B and the applied field H in the second quadrant of the B versus H hysteresis curve. Strnat reported the typical demagnetization curves for some important permanent magnets [5].

$(BH)_{max}$ is a quantity that measures the strength of a magnet of volume V , where V is inversely proportional to $(BH)_{max}$. So, a larger energy product means a stronger magnet, which implies that a smaller-sized magnet can be used according to the need for a specific application. **Figure 2** explains the idea for equal energy output for different materials having different volumes.

The theoretical value of the maximum energy product $(BH)_{max}$ can be given as

$$(BH)_{max,theoretical} = \frac{(B_s)^2}{4} = \frac{(4\pi M_s)^2}{4} \quad (1)$$

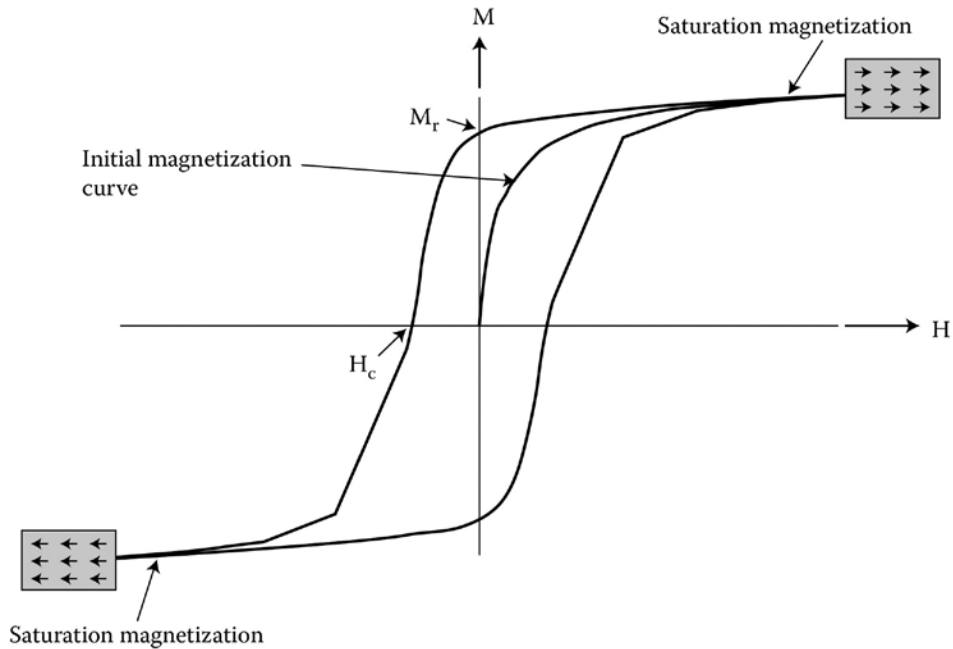


Figure 1. Typical hysteresis curve for a permanent magnet.

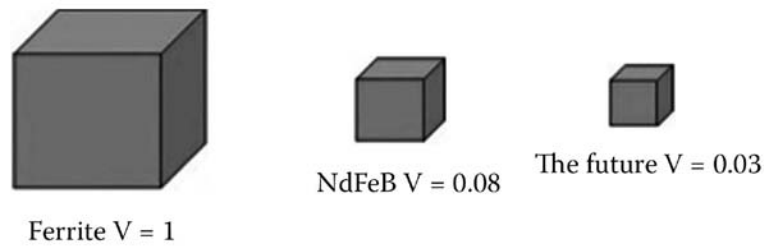


Figure 2. Equal energy output for materials having different volumes.

Figure 3 illustrates the demagnetization quadrant and the variation of the BH product for a typical permanent magnetic material [6]. Here OP is the load line and P is the working point of the magnet where the load line intersects with the demagnetizing B - H curve.

Figure 4 shows the time evolution of the maximum energy product in a logarithmic scale for different permanent magnets over the last century [7]. The theoretical potential should be considered. The material having the highest saturation magnetization can limit the theoretical $(BH)_{\max}$. The permanent magnet Nd - Fe - B has the highest theoretical energy product to be used in low-temperature applications and is already in large-quantity production in the United States [8]. The development of a hypothetical

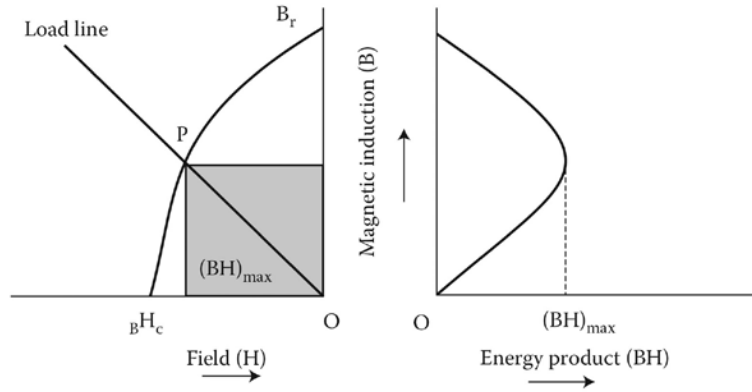


Figure 3. Demagnetization quadrant of a typical permanent magnet material and the variation of (BH) product with the demagnetizing field. (Adapted from R. A. McCurrie, *Ferromagnetic Materials—Structure and Properties*, Academic Press Limited, San Diego, CA, 1994, p. 193.)

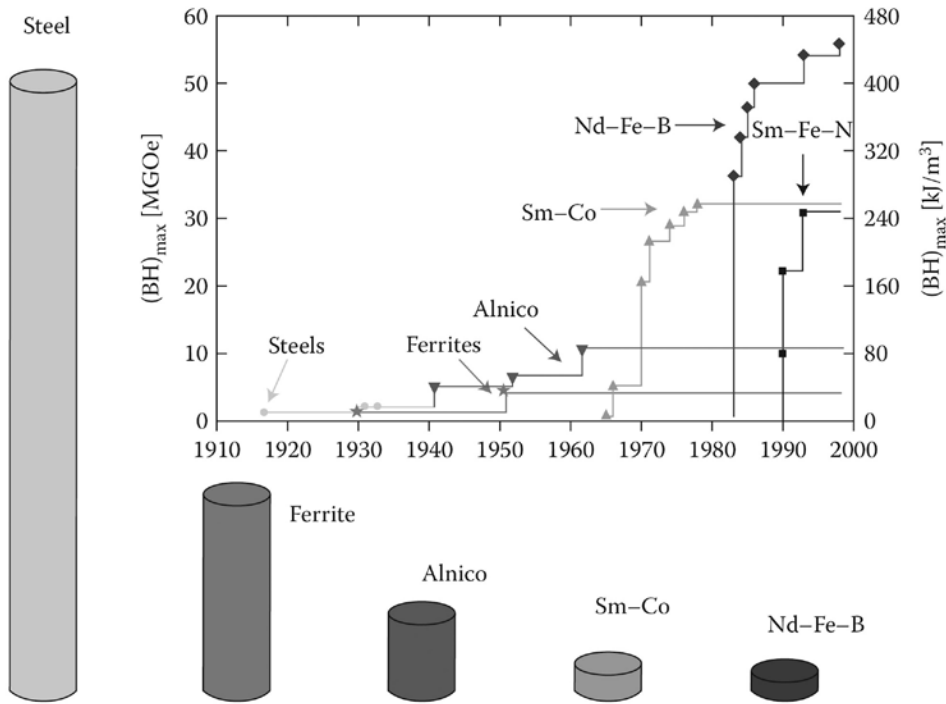


Figure 4. Development in the energy density $(BH)_{max}$ of hard magnetic materials in the twentieth century and presentation of different types of materials with comparable energy densities. (Reprinted with permission from O. Gutfleisch, *J. Phys. D Appl. Phys.* 33, 2000, R157–R172.)

Fe–Co-based high-energy magnet is under progress. An excellent $(BH)_{\max}$ value (500–1000 kJ/m³) could be achieved if the Fe–Co-based magnets with a large spontaneous polarization of 2.45 T could be realized by introducing strong planar pinning centers.

However, to avoid using relatively expensive and vulnerable sources of Co, the search for the Fe-based permanent magnets continued. This led to the discovery of Nd₂Fe₁₄B-based materials in 1983 [9–11], followed by interstitially modified Sm–Fe–N in 1992 [12–15]. But, both of these have some drawbacks compared to Sm–Co magnets. The Sm–Fe compounds are not useful as permanent magnet materials (for their basal plane easy magnetization direction) unless nitrogen diffusion expands the crystal structure and produces Sm₂Fe₁₇N_x. The Nd–Fe–B magnets are not applicable at higher temperatures. **Table 1** displays representative properties of various permanent magnet materials [7,16,17]. The properties have been tabulated with an increasing order of $(BH)_{\max}$.

The Nd-based alloys have comparatively low Curie temperatures than Sm-based alloys. Although Nd-based magnets are the strongest and the cheapest and are most widely used, Sm-based alloys are better in maintaining high magnetic strength at higher temperatures. Sm-based alloys have higher oxidation resistance than Nd-based alloys, although they are more prone to fracture from thermal shock. The various processing routes, related properties, and applications of those rare-earth magnets are discussed and compared in more detail later in the following sections of this chapter.

Table 1. Crystal Structures and Magnetic Properties of Various Permanent Magnets

| Magnet | Crystal Structure | B_r (T) | H_{ci} (kA/m) | $(BH)_{\max}$ (kJ/m ³) | T_c (°C) |
|---|-------------------|-----------|-----------------------|------------------------------------|------------|
| Sr-ferrite | Hexagonal | 0.2–0.4 | 100–300 | 10–40 | 450 |
| Ba-ferrite | Hexagonal | 0.38 MA/m | 110–320 | 10–45 | 450 |
| Alnico | Cubic | 0.2–1.4 | 55 | 10–88 | 700–860 |
| SmCo ₅ | Hexagonal | 0.8–1.1 | 600–2000 | 120–220 | 720 |
| Sm ₂ Co ₁₇ | Rhombohedral | 0.9–1.15 | 450–1300 | 150–340 | 830 |
| Pr ₂ Fe ₁₄ B | Tetragonal | 1.1–1.3 | 8.7 T ($\mu_0 H_A$) | 200–485 | 290–350 |
| Sm ₂ Fe ₁₇ N _x | Rhombohedral | 1.0–1.3 | 1050–2010 | 300–475 | 476 |
| Nd ₂ Fe ₁₄ B | Tetragonal | 1.0–1.4 | 750–2000 | 250–520 | 310–400 |

Source: From O. Gutfleisch, *J. Phys. D Appl. Phys.* 33, 2000, R157–R172; J. M. D. Coey, *J. Magn. Magn. Mater.* 248, 2002, 441–456; S. Aich, Crystal structure, microstructure and magnetic properties of SmCo-based permanent magnets, PhD dissertation, University of Nebraska, Lincoln, NE, 2005.

2 Various processing routes for rare-earth permanent magnets

The microstructure and the magnetic properties obtained for a magnetic material produced by a specific processing route are always correlated and are strongly dependent not only on the alloy composition but also on the processing parameters and heat treatments. The melt-spun ribbons of SmCo-based alloys produced by rapid solidification exhibited higher intrinsic properties, improved microstructures, and better magnetic properties ($M_r \sim 8.5$ kG, $H_c \sim 4.1$ kOe, $(BH)_{\max} \sim 18.2$ MGOe, and a high remanence ratio of 0.9) [18]. Zr and Cu substitution for Co helped to reduce the crystallographic texture, and $\text{Sm}(\text{Co}_{0.74}\text{Fe}_{0.1}\text{Zr}_{0.04}\text{Cu}_{0.12})_{8.5}$ ribbons were nearly isotropic [19]. In magnetically anisotropic SmCo_5 ribbons, well-crystallized grains with hexagonal structure (P6/mmm) were observed. Due to the addition of Fe in SmCo_5Fe_x ($x = 0, 1, \text{ and } 2$) melt-spun ribbons, produced by using a wheel speed of 25 m/s, the highest magnetic properties were observed for $x = 2$ ribbons due to their lowest content of Sm-rich phase and the smallest grain size [20]. Due to higher surface-to-volume ratio for $x = 2$, the intergrain exchange coupling enhanced the remanence. Improved magnetic properties (coercivity as high as 38.5 kOe) were reported for the melt-spun $\text{Sm}(\text{Co}_{0.74-x}\text{Fe}_{0.1}\text{Cu}_{0.12}\text{Zr}_{0.04}\text{B}_x)_{7.5}$ ($x = 0.005\text{--}0.05$) alloys [21]. Better magnetic properties were reported for the boron-containing samples than the carbon-containing samples in melt-spun $\text{Sm}(\text{CoFeCuZr})_2\text{M}_x$ ($M = \text{B or C}$) nanocomposite magnets due to the finer grain size (30–50 nm) of the former [22].

Depending on the microstructure scale (grain size), the basic processing routes for the magnet production can be classified as either microcrystalline or nanocrystalline route [23]. The microcrystalline route follows the powder metallurgy technique and eventually provides anisotropic magnets having a maximum energy product as high as 50 MGOe, whereas the nanocrystalline route involves rapid solidification techniques (melt spinning or atomization) and other alternate routes (hydrogenation–disproportionation–desorption–recombination [HDDR] or mechanical alloying), which eventually results in isotropic ($(BH)_{\max} \sim 10\text{--}15$ MGOe) and anisotropic magnets ($(BH)_{\max} \sim 20\text{--}40$ MGOe). **Figure 5** shows the schematic of the basic processing routes for permanent magnet productions.

In the following sections, each of the common processing routes is described in brief.

2.1 Powder metallurgy route

For a long time, it has been a general trend to use powder metallurgy technique to produce anisotropic sintered magnets. Certain conditions are necessary to be fulfilled during the production of anisotropic sintered magnets using the powder metallurgy route [24–26]:

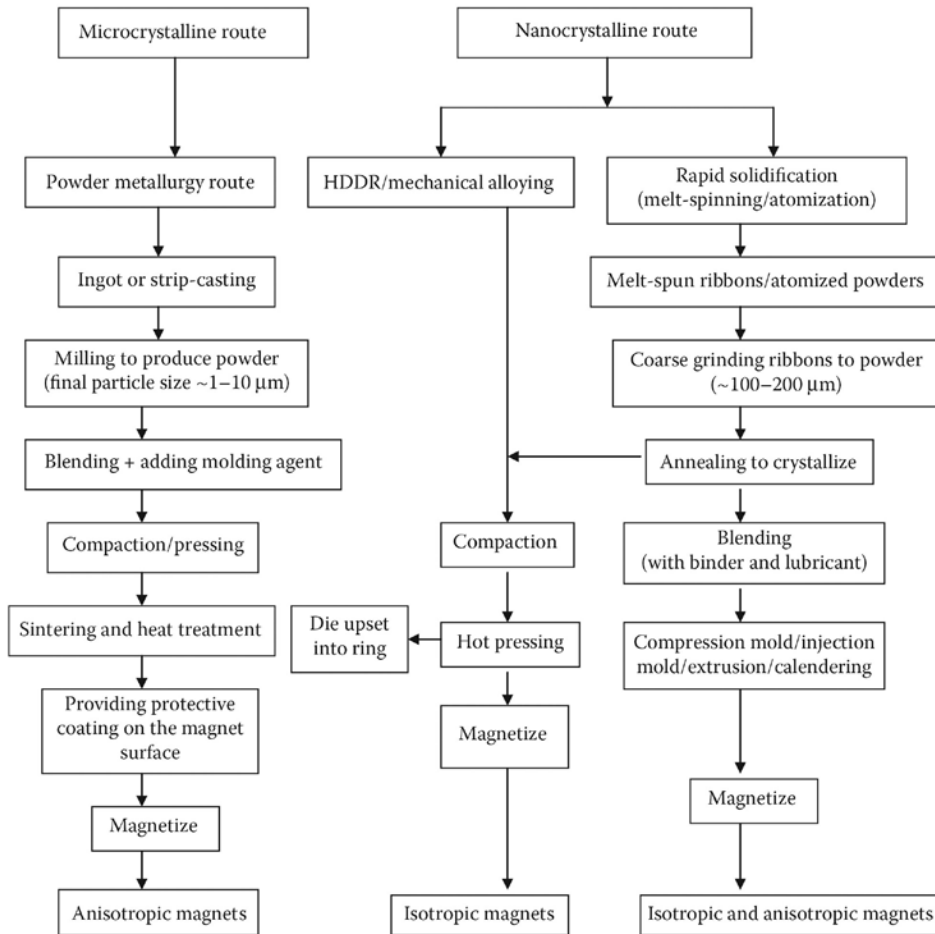


Figure 5. Schematic of the common processing routes (block diagram/flow chart). (From D. Brown, B.-M. Ma, and Z. Chen, *J. Magn. Magn. Mater.* 248, 2002, 432–440.)

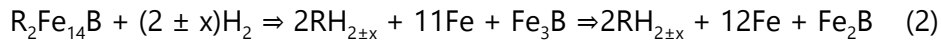
1. The oxygen content should be minimized.
2. The hard magnetic phase should be in a high-volume fraction.
3. The volume fraction of the nonmagnetic grain boundary material should be minimized.
4. A small crystallite size with narrow size distribution is required (for $\text{Nd}_2\text{Fe}_{14}\text{B}$ -type magnet typically 2–6 μm).
5. Maximum alignment of the easy axis of magnetization of the crystallites should be maintained.

However, further discussion of the powder metallurgy route is out of the scope of this chapter.

2.2 Hydrogen-assisted processing

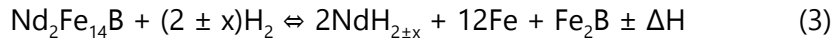
2.2.1 Hydrogenation–disproportionation–desorption–recombination

The HDDR process is a well-known processing route for achieving the refined grain structure in the case of rare-earth transition-metal alloys (especially in Nd–Fe–B alloys). This process is very simple and mainly based on hydrogen-induced phase transformation, which can produce highly coercive $\text{Nd}_2\text{Fe}_{14}\text{B}$ powders that can be used to produce bonded magnets as well as fully dense hot-pressed magnets. The principal HDDR reaction of the $\text{R}_2\text{Fe}_{14}\text{B}$ phases can be mentioned as [27]



where R = Nd or Pr. During HDDR of $\text{Pr}_{13.7}\text{Fe}_{63.5}\text{Co}_{16.7}\text{Zr}_{0.1}\text{B}_6$ alloy, an intermediate boride phase, $\text{Pr}(\text{Fe},\text{Co})_{12}\text{B}_6$ (R3m), has also been found after disproportionation [28]. Also, a high degree of texture has been reported for this type of alloy after conventional processing [29].

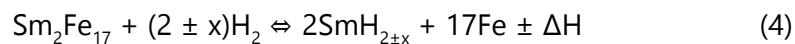
The HDDR reaction in the Nd–Fe–B system can be expressed as [30]



The whole reaction occurs in two stages:

1. *Stage I—Disproportionation:* $\text{Nd}_2\text{Fe}_{14}\text{B}$ phase decomposes into a finely divided mixture of neodymium hydride (NdH_2), iron (Fe), and ferro-boron (Fe_2B). The reaction occurs at $\sim 800^\circ\text{C}$ and at 1 bar hydrogen pressure.
2. *Stage II—Desorption and Recombination:* During desorption due to subsequent heat treatment under vacuum, hydrogen removal occurs from NdH_2 and the disproportionated NdH_2 , Fe, and Fe_2B are recombined into $\text{Nd}_2\text{Fe}_{14}\text{B}$ phase with much finer grain structure. The HDDR process for Nd–Fe–B alloy is shown in **Figure 6**.

The application of HDDR-processed $\text{Sm}_2\text{Fe}_{17}\text{N}_3$ magnets is restricted to bonded magnets only because of their insufficient thermal stability (stable only up to 600°C) [7]. However, the thermal stability can be improved using $\text{Sm}_2\text{Fe}_{17-x}\text{Ga}_x\text{C}_y$ alloy [31]. The reaction in HDDR-processed $\text{Sm}_2\text{Fe}_{17}\text{N}_3$ system can be expressed as [7]



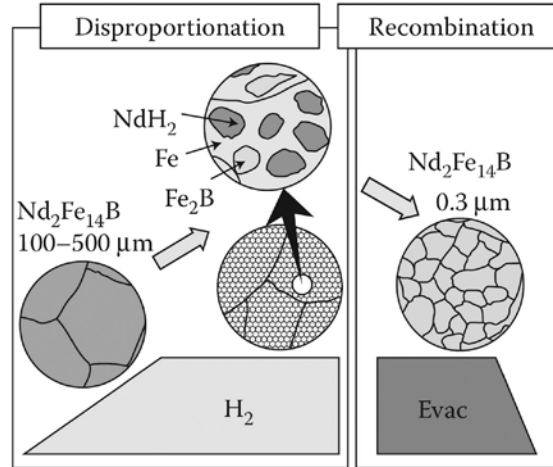
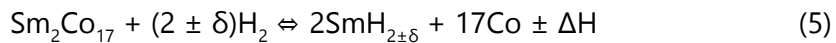


Figure 6 Schematic of HDDR process in NdFeB system. (Reprinted with permission from S. Sugimoto, *J. Phys. D Appl. Phys.* 44, 2011, 064001.)

The advantage of the HDDR process over melt spinning is production of anisotropic powders by aligning the c-axis of $\text{Nd}_2\text{Fe}_{14}\text{B}$ along one direction by changing the composition (addition of alloying elements) or by adjusting the process parameters (controlling the hydrogen pressure and temperature) of the HDDR process.

2.2.2 Reactive milling in hydrogen

In this special technique, mainly ball milling is done (under enhanced hydrogen pressure and temperature) for disproportionation, which is followed by vacuum annealing for desorption and recombination. Gutfleisch reported the effect of reactive milling on $\text{Sm}_2\text{Co}_{17}$ alloy [7]. The following reaction occurs during reactive milling like the HDDR-processed $\text{Sm}_2\text{Fe}_{17}$ alloy mentioned earlier:



The average grain size of rare-earth hydride phase (SmH) obtained in this process was much smaller (~ 9 nm) [32] compared to the same obtained during disproportionation of the conventional HDDR process [33,34]. Finally, the average grain size was dependent on the recombination temperature; the observed grain size was estimated as ~ 18 , ~ 25 , and ~ 29 nm at 600°C , 650°C , and 700°C recombination temperatures, respectively [35]. The remanence value ($J_r = 0.71$ T) was also significantly higher (for the sample

recombined at 600°C) compared to the theoretical value ($J_s/2 = 0.65$ T) of single-domain $\text{Sm}_2\text{Co}_{17}$ particles because of the strong exchange interaction between the nanosized grains in the former case. The higher remanence enhancement was observed in the case of $\text{Nd}_2\text{Co}_{14}\text{B}$ alloys due to their smaller grain size obtained during reactive milling (disproportionation) of a series of $\text{Nd}_2(\text{Fe,Co})_{14}\text{B}$ alloys [36].

Finally, the HDDR processing of R–T compounds (R_nT_m) is an alternative route to mechanical alloying, intensive milling, or rapid quenching for the synthesis of amorphous or nanocrystalline materials. The nature of the final product of the process depends on the thermodynamics and kinetics of the whole process [7,37]. Thermodynamics includes stabilities of the starting alloy and reaction products, and kinetics includes temperature, hydrogen pressure, and possibly mechanical activation. Depending on the thermodynamics and the kinetics, the final product can be an interstitial modified ternary hydride (crystalline [$c\text{-R}_n\text{T}_m\text{H}_x$] or amorphous [$a\text{-R}_n\text{T}_m\text{H}_x$]) [7] or a binary R hydride and the T ($n\text{RH}_x + m\text{T}$) as a result of disproportionation (**Figure 7**).

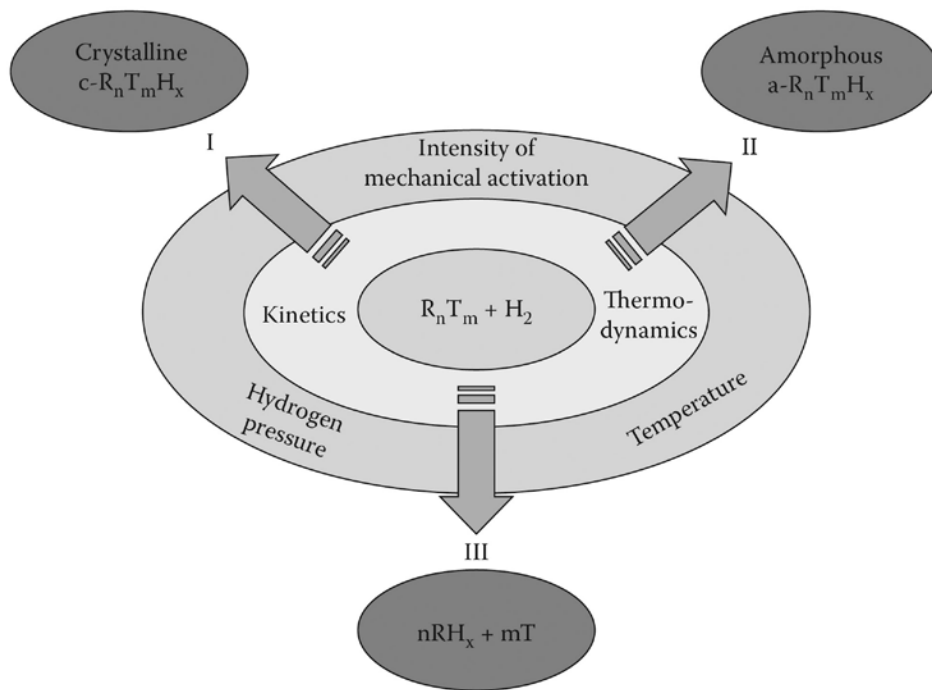


Figure 7. Schematic representation of hydrogen gas–solid reactions of R–T compounds. Depending on thermodynamics and kinetics, a ternary hydride (I, $c\text{-R}_n\text{T}_m\text{H}_x$), an amorphous hydride (II, $a\text{-R}_n\text{T}_m\text{H}_x$), or a binary R hydride and the T (III, $n\text{RH}_x + m\text{T}$) is formed. (Reprinted with permission from O. Gutfleisich, *J. Phys. D Appl. Phys.* 33, 2000, R157–R172.)

2.3 Mechanical alloying

Mechanical alloying uses a high-energy ball milling followed by a suitable annealing treatment. In this process, mixing of different elements occurs through an interdiffusional reaction resulting in the formation of ultrafine layered structure of composite particles. The feasibility of alloy formation depends on several factors, such as (i) thermodynamics of the alloy system, (ii) mechanical workability of the starting materials (powders), and (iii) the input energy used during the ball milling process. Because mechanical alloying is a nonequilibrium processing technique, it can overcome many limitations of the conventional milling processes. Like the other nonequilibrium processes (such as rapid solidification), it helps to form the metastable phases during processing. During mechanical alloying of Nd–Fe–B magnets, initially during ball milling, a layered structure of Nd and Fe is formed with undeformed B particles embedded along the interfaces [7]. Subsequent annealing at low temperatures (600–700°C) for relatively short times (10–30 minutes) for the ultrafine and homogeneously distributed reactant particles results in the formation of the Nd₂Fe₁₄B hard magnetic phases. Several rare-earth transition-metal (R–T) compounds, such as SmFeTi [38], SmCoFe [39], SmFeN [40,41], SmFeGaC [42], and Sm–Co [43], were synthesized by mechanical alloying routes using elemental powders as precursors. The as-milled structures of all of the compounds consist of nanocrystalline α -Fe and an R-rich phase, except the Sm–Co compound where a single amorphous phase of SmCo₅ was formed. Subsequent annealing of the as-milled products forms nanocrystalline structure of all those compounds with crystallite size of 10–50 nm. Gutfleisch reported a modified version of mechanical alloying process called “intensive milling technique” where alloy powder is used instead of elemental powder during high-energy ball milling [7]. Coercivity of an intensively milled powder is relatively higher than the same obtained through mechanical alloying [44]. Nanostructured PrCo₅ powders synthesized by intensive milling for 4 hours and subsequent annealing at 800°C for 1 minute resulted in a coercivity of 16.3 kOe [45]. The nanocrystalline Nd₁₂Fe₈₂B₆ alloy powders prepared by HDDR and mechanical milling present high magnetic properties that can be attributed to the exchange coupling between the nanosized Nd₂Fe₁₄B and α -Fe phases [46].

Among all the aforementioned processing routes, rapid solidification technique (rapid solidification processing [RSP]) is the most favorable route to produce permanent magnets because not only does it (RSP) produce the ultrafine grain size (nanostructure), but it also provides better chemical homogeneity and some desirable nonequilibrium metastable phases. The next section discusses various rapid solidification techniques as well as the principles and the advantages and disadvantages of those techniques.

2.4 Rapid solidification techniques

RSP is becoming a more important area in solidification and has significant potential in industrial use. It can be considered as nonequilibrium cooling as the cooling rate or solidification rate is very high here ($\sim 10^3\text{--}10^9$ K/s). In any RSP technique, the rate of advancement of the solidification front (solid/liquid interface) “ V ” is greater than 1 cm/s. During rapid solidification, as it is a nonequilibrium cooling, loss of local equilibrium occurs at the solid/liquid interface. Due to the interfacial nonequilibrium, the equilibrium phase diagram fails at the interface and the chemical potentials of liquid and solid are not equal anymore. The situation has been described schematically in **Figure 8** along with related chemical potential gradients.

When the growth rate (V) is comparable or larger than the rate of diffusion over an interatomic distance (D_i/δ_i), that is, $V \geq D_i/\delta_i$, the crystal/atom will not have time to change its composition (rearrange themselves) at the interface so as to equalize the chemical potential (μ) of both phases ($\mu_s \neq \mu_l$), which results in “solute trapping.”

Rapidly solidified permanent magnets are getting much more attention since the last decade because of their significantly less complicated processing routes compared to the time-consuming and complicated heat treatment and solution treatment, which is normally required to achieve a remarkably high coercivity for bulk rare-earth permanent magnets. Among

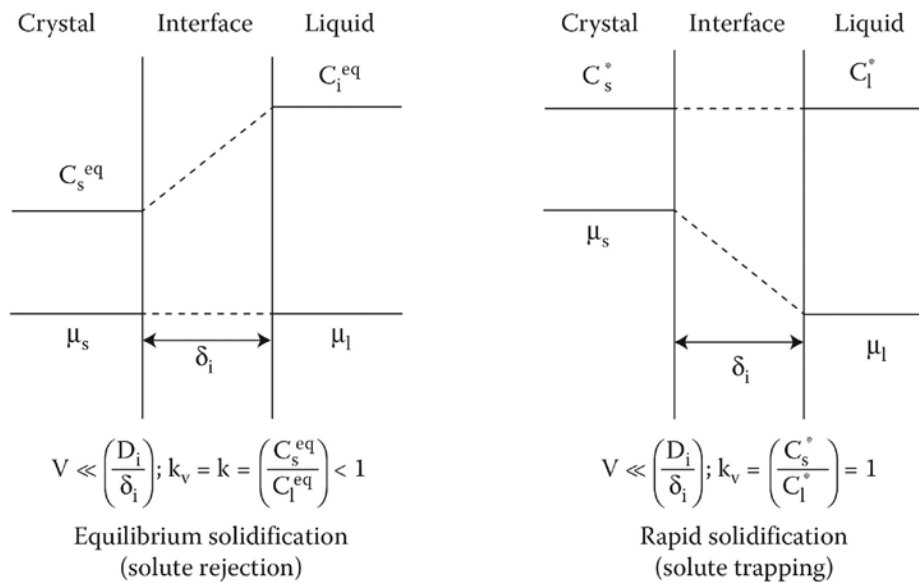


Figure 8. Loss of local equilibrium at the solid–liquid interface due to the increase in solidification rate/undercooling.

the several advanced rapid solidification techniques such as melt atomization, thermal spray coatings, melt spinning, laser melting and resolidification, and high-energy beam treatment of surfaces, melt spinning is the most commonly used rapid solidification technique for the processing of rare-earth permanent magnet alloy systems. The other techniques have specific advantage(s) with added disadvantage(s); for example, the atomization technique provides high production rate and uniform spherical particle morphology, but cannot provide the compositional changes required by the lower cooling rate involved [23]. Various techniques that can be used to produce rapidly solidified alloys can be categorized as the following:

1. Melt spinning, planar flow casting, or melt extraction, which produce thin ($\sim 25\text{--}100\ \mu\text{m}$) ribbon, tape, sheet, or fiber
2. Atomization, which produces powder ($\sim 10\text{--}200\ \mu\text{m}$)
3. Surface melting (by laser) and resolidification, which produce thin surface layers

Figure 9 shows the schematics of various RSP techniques. Each of the categories is discussed in brief in the following sections.

2.4.1 Atomization

Atomization is a technique that uses high-pressure fluid jets to break up a molten metal stream into very fine droplets, which eventually solidify into fine particles. This is a versatile method for powder production. High-quality powders of different metals and alloys, such as aluminum, brass, iron, stainless steel, tool steel, and superalloys, are produced in this method.

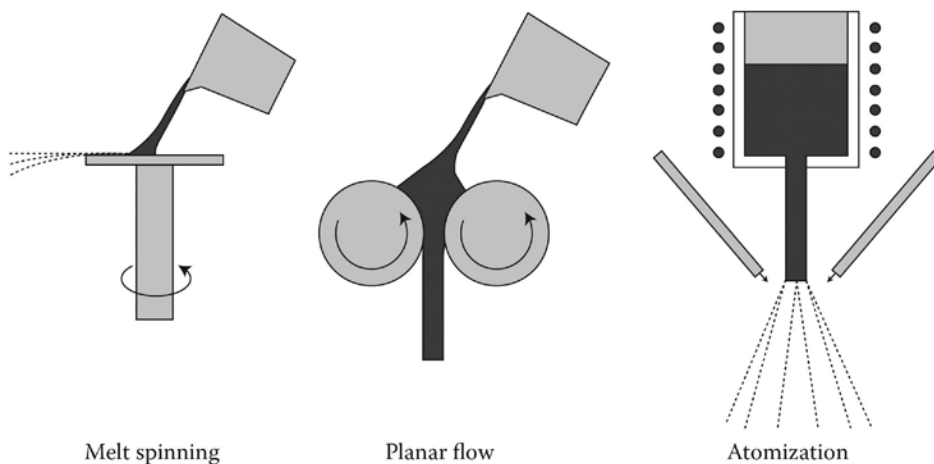


Figure 9. Schematics of some common RSP techniques.

The important *objectives* of atomization are as follows:

- Minimization of the average particle size
- Reduction of the particle size distribution width
- Technical production of complex melt systems for powder applications

2.4.1.1 Various Atomization Processes

Various atomization processes are available depending upon the atomizing medium to break up the liquids, requirements of powder characteristics, and related cost. Different types of atomization processes can be mentioned as follows:

- Water atomization
- Gas atomization
- Soluble gas or vacuum atomization
- Centrifugal atomization
- Rotating disk atomization
- Ultrarapid solidification process
- Ultrasonic atomization

Among all of the atomization techniques mentioned above, water atomization and gas atomization techniques are very popular and are mostly used (**Figure 10**) [47].

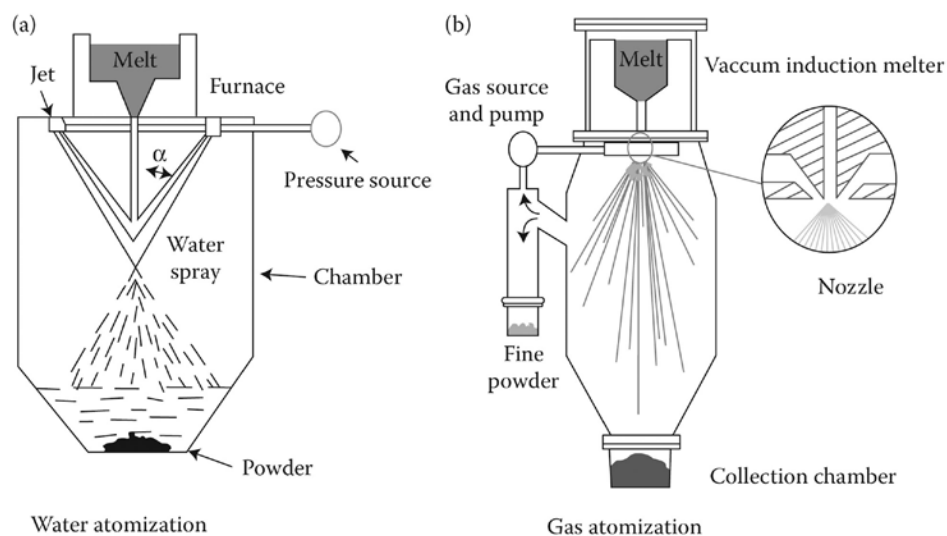


Figure 10. Schematics of atomization techniques: (a) water atomization and (b) gas atomization. (Adapted from R. M. German, *Powder Metallurgy Science*, 2nd ed., Metal Powder Industries Federation (MPIF), Princeton, NJ, 1994, ISBN-13: 978-1878954428.)

2.4.1.2 Mechanism of atomization

In conventional (gas or water) atomization, a liquid metal is produced by pouring molten metal through a tundish with a nozzle at its base (a reservoir used to supply a constant, controlled flow of metal into the atomizing chamber). As the metal stream exits the tundish, it is struck by a high-velocity stream of the atomizing medium (water, air, or an inert gas). The molten metal stream is disintegrated into fine droplets, which solidify during their fall through the atomizing tank. Particles are collected at the bottom of the tank. Alternatively, centrifugal force can be used to break up the liquid as it is removed from the periphery of a rotating electrode or spinning disk/cup. The disintegration of liquid stream is shown in **Figure 11**. This has five stages: (i) formation of wavy surface of the liquid due to small disturbances (blobs); (ii) wave fragmentation and ligament formation (ligaments are non-spherical liquid sheets, sheared off the liquid jet column); (iii) disintegration of ligament into fine droplets; (iv) further breakdown of fragments into fine particles; and (v) collision and coalescence of particles.

Additional alloying can be performed in the liquid metal bath after the original charge has become molten. Also, the bath can be protected from oxidation by maintaining an inert gas atmosphere as a cover over the liquid metal. Alternatively, the top of the furnace can be enclosed in a vacuum chamber. The furnace type and degree of protection are determined by the chemical composition of the bath and the tendency of the metal to oxidize. **Table 2** compares the shape and size of the particles obtained from different atomization techniques and cooling rates.

2.4.2 Surface melting by laser and resolidification

Use of laser in material processing is attributed to the way it interacts with the materials (especially with the material surface). The laser-matter

Table 2. Particle Shape, Particle Size, and Cooling Rates for Various Atomization Techniques

| <i>Process/Technique</i> | <i>Particle Shape</i> | <i>Average Particle Size (μm)</i> | <i>Cooling Rate (K/s)</i> |
|--|-----------------------|---|---------------------------|
| Water atomization | Irregular | 75–200 | 10^2 – 10^4 |
| Gas atomization (ultrasonic) | Spherical | 10–50 | $\geq 10^6$ |
| Vacuum atomization (gas soluble) | Spherical | 20–150 | 10^2 – 10^4 |
| Centrifugal atomization (rotating electrode) | Spherical | 150–250 | 10^4 – 10^6 |
| Rotating disk atomization | Spherical | Variable (depending on disk speed) | |

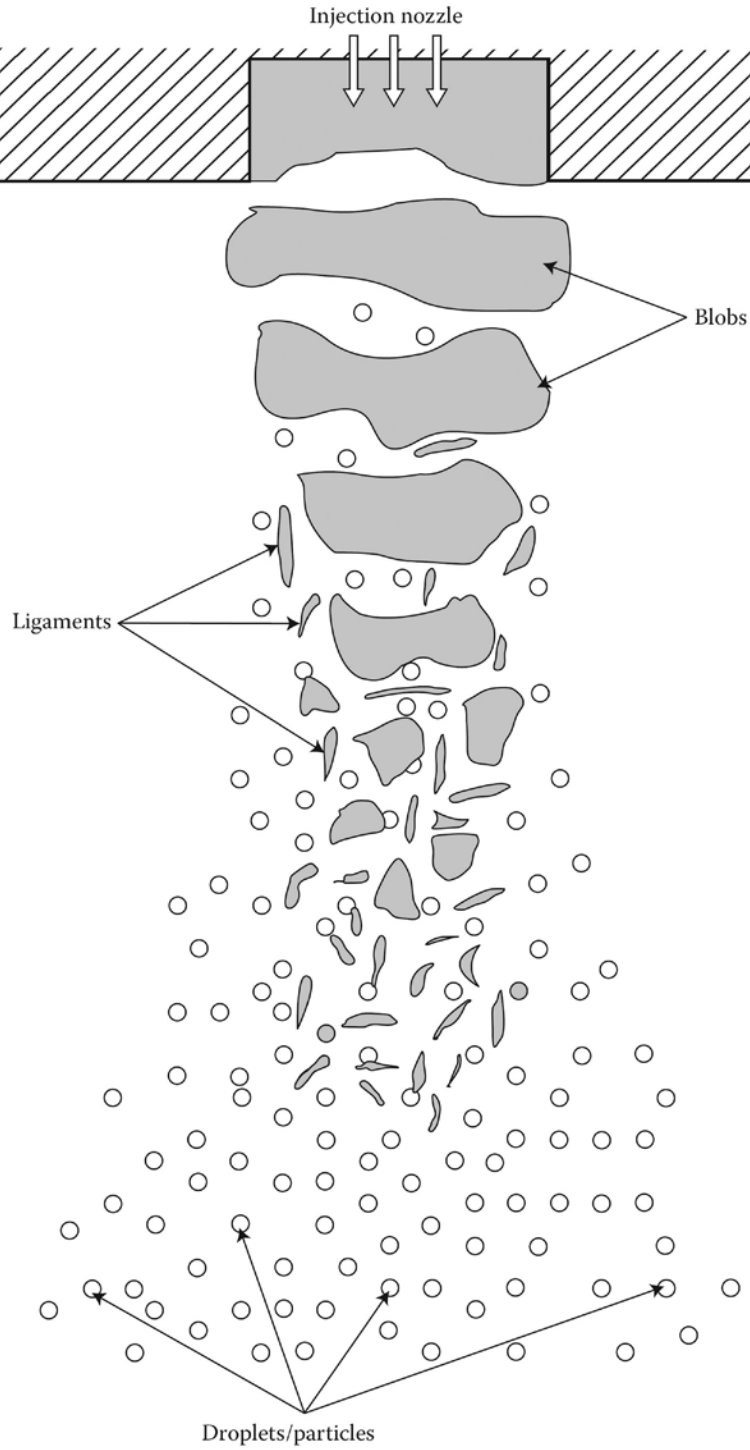


Figure 11. Schematic of the disintegration of the liquid stream during atomization.

interaction within the near-surface region achieves extreme heating and cooling rates (10^3 – 10^{10} K/s), while the total deposited energy (~ 0.1 – 10 J/cm²) is insufficient to affect the temperature of the bulk material. This allows the near-surface region to be processed under extreme conditions with little effect on the bulk properties.

2.4.2.1 Laser rapid prototyping

One of the most recent applications of laser in material processing is development of rapid prototyping technologies, where lasers have been coupled with computer-controlled positioning stages and computer-aided engineering design to enable new capability [48–55]. This development implies that manufacturers are no longer constrained to shape metals by the removal of an unwanted material. Instead, components can now be shaped into near-net-shape parts by addition/building the object in lines or layers one after another. Rapid prototyping relies on “slicing” a three-dimensional computer model to get a series of cross sections that can then be made individually. The major techniques for making the slices are stereolithography, selective laser sintering (SLS), laminated object manufacturing, and fused deposition modeling. Laser can be a useful tool for *in situ* rapid prototyping fabrication of composite components such as cutting tools, shear blades, and so on [54].

2.4.2.2 Selective laser melting

Selective laser melting (SLM) is a powder-based additive manufacturing (AM) process that allows obtaining fully functional three-dimensional parts from a CAD model, able to produce functional components from materials having mechanical properties comparable to those of bulk materials. The competitive advantages of the AM process are geometrical freedom, shortened design to product time, reduction in process steps, mass customization, and material flexibility. SLM refers to the direct route of SLS when complete melting of powder occurs rather than sintering or partial melting. During the process, successive layers of metal powder are fully molten and consolidated on top of each other by the energy of a high-intensity laser beam (**Figure 12**) [56]. Consequently, almost fully dense parts with no need for post-processing other than surface finishing are produced. The important applications in this area include customized medical parts, tooling inserts with conformal cooling channels, and functional components with high geometrical complexity. SLM is characterized by high-temperature gradients, causing no equilibrium to be maintained at the solid/liquid interface, thereby leading to rapid solidification as the melt pool undergoes transformation from liquid to solid. Formation of nonequilibrium

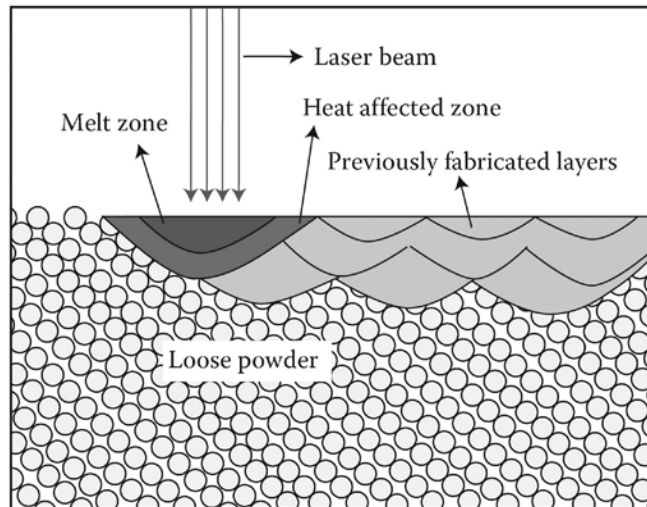


Figure 12. Schematic view of the transverse section showing different zones due to the process. (Adapted from J. P. Kruth et al., *Proceedings of the 16th International Symposium on Electro-Machining*, 2010.)

phases and grain refinement are the basic characteristics of this process. Grain structure in SLM differs from the conventional manufacturing process not only because of the cooling rate but also due to the grain structure of the previously solidified layer and the SLM parameters resulting in different (improved) mechanical properties, such as yield strength, ductility, and hardness [56].

Although the objective in SLM is often to obtain 100% dense parts, the goal is difficult to achieve since there is no mechanical pressure, as in molding processes. SLM is characterized only by temperature effects, gravity, and capillary forces during SLM. Moreover, gas bubbles can become entrapped in the material during the solidification due to various causes, such as decrease in the solubility of the dissolved elements in the melt pool during solidification. Besides those melting and solidification phenomena, an insufficient surface quality can cause low density as well. Moreover, the laser energy may not be enough to melt the new layer completely since the depth of the powder in some regions will be thicker. Sometimes, a rough surface causes the entrapment of gas upon deposition of a new powder layer. When the new layer is being scanned, the gas is superheated and expands rapidly removing the liquid metal above it, thus creating a pore.

Building axis: So, the idea for remelting arrives. Laser remelting can improve the density when compared to parts made without remelting. The average porosity of parts without remelting is about 0.77% whereas the

densest re-molten part obtained has a porosity of 0.032%. Higher remelting scan speed (200 mm/s) in combination with low laser power (85 W) resulted in better density values. Applying remelting once or multiple times after each layer does not significantly change the porosity for low laser energy inputs to the substrate.

2.4.3 Electrospinning

Electrospinning has been recognized as an efficient technique for the fabrication of polymer nanofibers [57]. Various polymers have been successfully electrospun into ultrafine fibers in recent years, mostly in solvent solution and some in melt form. Potential applications based on such fibers, specifically their use as reinforcement in nanocomposite development, have been realized. However, what makes electrospinning different from other nanofiber fabrication processes is its ability to form various fiber assemblies. This will certainly enhance the performance of products made from nanofibers and allow application-specific modifications. It is therefore vital for us to understand the various parameters and processes that allow us to fabricate the desired fiber assemblies. Fiber assemblies that can be fabricated include nonwoven fiber mesh, aligned fiber mesh, patterned fiber mesh, random three-dimensional structures, and submicron spring and convoluted fibers. Nevertheless, more studies are required to understand and precisely control the actual mechanics in the formation of various electrospun fibrous assemblies.

2.4.4 Melt spinning

Melt spinning is one of the most commonly used rapid solidification techniques. People started to use this technique in 1872 with a simple version of melt spinning to produce wires of low-melting temperature alloys [58]. Later, some improved versions of the melt-spinning technique such as chill-block melt spinning (1908) (the precursor of modern single-roller melt spinning) and free-flight melt spinning (1961) (where a jet of molten alloy, coming out of a nozzle, is quenched by the surrounding gas, while it is still in flight) have been invented. The most recent improvement is the single-roller device (the modern version of the chill-block melt spinning), which has been described by Anantharaman and Suryanarayana [59,60]. This device can be used in the most sophisticated way where one or more melt streams are used to make wide or composite ribbons by impingement on single or twin chill roll surfaces [61]. **Figure 13** represents an RSP unit.

Here the molten metal is ejected through a small bore at the bottom of a quartz crucible on the surface of a rotating Cu wheel. When the red-hot

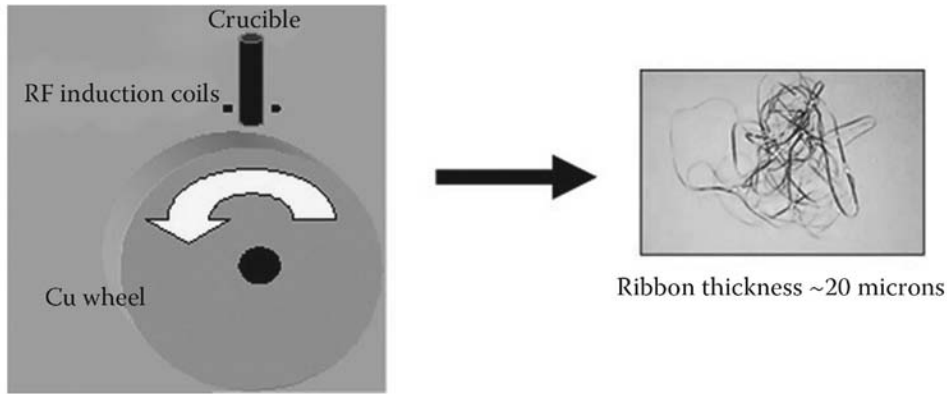


Figure 13. Schematic of rapid solidification unit/principle.

molten metal touches the chilled surface of the rotating Cu wheel, the molten pool transforms to a thin ribbon due to very high cooling rate and the ribbons leave the wheel surface tangentially to a collecting chamber from where the final products (the melt-spun ribbons) are collected.

The melt-spun ribbons of SmCo alloys produced by rapid solidification exhibited higher intrinsic properties, improved microstructures, and better magnetic properties ($M_r \sim 8.5$ kG, $H_c \sim 4.1$ kOe, $(BH)_{\max} \sim 18.2$ MGOe, and a high remanence ratio of 0.9). Some of the other rapid solidification techniques mentioned above have been tried many times on Nd–Fe–B systems, but rarely on Sm–Co systems because of the high vapor pressure of Sm, making it difficult to control the composition. (Sm–Co was gas atomized a long time ago. A company called Crucible Industries worked on it.)

The advantages of the melt-spinning technique (as a rapid solidification technique) over the other solidification techniques on phase equilibria and microstructure of the materials can be mentioned as follows:

- The reduction of grain size as the cooling rate increases to achieve the typical scale (nanoscale) of microstructure
- Better chemical homogeneity with increasing cooling rate
- Production of nonequilibrium metastable crystalline phases
- Extension of solubility and homogeneity ranges of equilibrium phases as the cooling rate increases
- The formation of nonequilibrium glassy phases due to failure of the liquid to undergo complete crystallization

The kinetics of rapid solidification during melt-spinning technique is described in the following few lines. The fundamental feature of melt spinning related to the kinetics of rapid solidification is that the heat evolved during

solidification must be transferred with sufficient rapidity to a heat sink, which involves the propagation of a solidification front at a high velocity. The typical cooling rate obtained in this method is $\sim 10^5\text{--}10^6$ K/s.

In **Figure 14**, three typical conditions have been considered: a molten sphere of radius " r " traveling in a cool gaseous medium (droplet rapid solidification process), a molten cylinder of radius r injected into a bath of liquid coolant (in production of rapidly solidified wire), or a parallel-sided slab of melt of thickness z in at least partial contact on one side with a chill substrate (chill-block melt spinning).

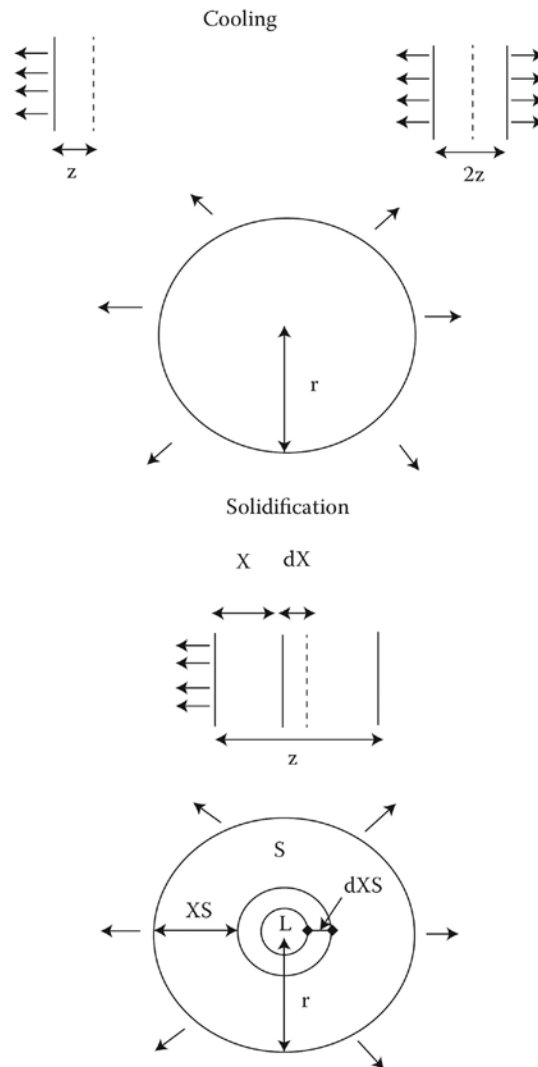


Figure 14. Cooling and solidification of a sphere or a cylinder or a slab. The arrows are indicating the direction of heat extraction. (Adapted from N. J. Grant, H. Jones, and E. J. Lavernia, *Elements of Rapid Solidification—Fundamentals and Applications*, M. A. Otooni (ed.), p. 35.)

Assuming the interfacial heat-transfer coefficient h is sufficiently low to maintain an essentially uniform temperature throughout the sphere or slab or cylinder during cooling and solidification, the cooling rate (\dot{T}) can be expressed as the following

$$\dot{T} = -\frac{dT}{dt} = \frac{h(T - T_A)}{c\rho} \frac{A_0}{V_0} \quad (6)$$

where A_0 is the surface area losing heat, V_0 and ρ are the volume and the density, respectively, T_A is the final temperature after the heat lost to the gas, liquid coolant, or chill-block, and c is the specific heat released during a small increase in temperature dT to the heat removed in a corresponding time increment dt . Here A_0/V_0 is $3/r$, $2/r$, and $1/z$ for a sphere, a cylinder, and a slab, respectively. The average solidification front velocity (\dot{X}) can be given as

$$\dot{X} = -\frac{dX}{dt} = \frac{h(T_F - T_A)}{L\rho} \frac{A_0}{A_F} \quad (7)$$

where L is the latent heat released at T_F , the freezing temperature of the melt, and A_F is the instantaneous area of the solidification front at position X and A_0/A_F is $r^2/(r - x)^2$, $r/(r - x)$, and 1 for the sphere, the cylinder, and the slab, respectively.

2.4.5 Melt extraction

The melt-extraction process is an RSP technique, which yields short metal fibers with equivalent diameters as low as 50 μm from almost arbitrary metals and alloys [62]. Smooth and uniform cross-section fibers with relatively high tensile strength can be obtained from the process depending on the process parameter. Generally, the melt-extraction process is divided into two subdivisions (**Figure 15**): (1) crucible melt extraction (CME) and (2) pendant drop melt extraction (PDME). Both the subdivisions individually as well as in combination are very beneficial for producing amorphous glassy ribbon.

In the following section and subsections, a detailed discussion is performed on the basis of processing, properties, and applications of various rapidly solidified permanent magnets, such as R-Co-based magnets, R-Fe-B-based systems, and R-Fe-T-based alloys, where R is the rare-earth and T is mainly the C and N.

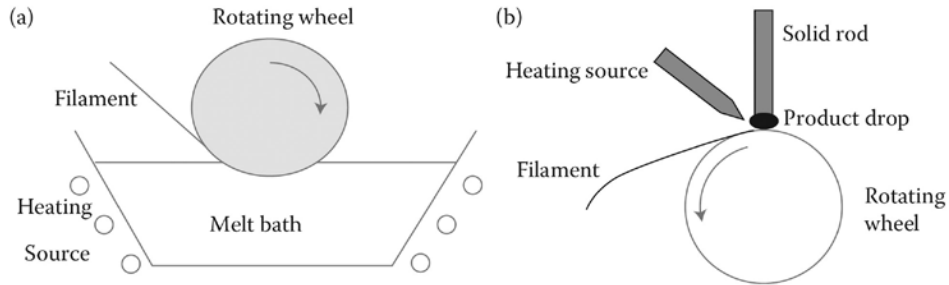


Figure 15. Schematic of (a) CME and (b) PDME.

3 Rapidly solidified rare-earth permanent magnets

Rapidly solidified permanent magnets are getting much more attention since the last decade because of their significantly less complicated processing routes compared to the time-consuming and complicated heat treatment and solution treatment, which is normally required to achieve a remarkably high coercivity for bulk rare-earth permanent magnets. Among the several advanced rapid solidification techniques such as melt atomization, thermal spray coatings, melt spinning, laser melting and resolidification, and high-energy beam treatment of surfaces, melt spinning and melt atomization are the most commonly used rapid solidification techniques for the processing of rare-earth permanent magnet alloy systems. The melt-spun ribbons of Sm–Co alloys produced by rapid solidification exhibited higher intrinsic properties, improved microstructures, and better magnetic properties ($M_r \sim 8.5$ kG, $H_c \sim 4.1$ kOe, $(BH)_{\max} \sim 18.2$ MGOe, and a high remanence ratio of 0.9). Some of the other rapid solidification techniques mentioned earlier have been tried on Nd–Fe–B systems, but not on Sm–Co systems because of the high vapor pressure of Sm, making it difficult to control the composition. Several advantages of the melt-spinning technique as a rapid solidification technique over the other solidification techniques are reduction of grain size to achieve the typical scale (nanoscale) of microstructure, better chemical homogeneity, production of nonequilibrium metastable crystalline phases, and the formation of nonequilibrium glassy phase. The fundamental feature of the melt-spinning technique related to the kinetics of rapid solidification is that the heat evolved during solidification must be transferred with sufficient rapidity to a heat sink, which involves propagation of a solidification front at a high velocity. The typical cooling rate obtained in this method is $\sim 10^5$ – 10^6 K/s. In the following subsections, we discuss the processing, structure, properties, and applications of some important permanent magnets, such as R–Co-based (Sm–Co-based, Pr–Co-based) magnets, R–Fe–B (Nd–Fe–B, Pr–Fe–B) magnets, and SmFeN/SmFeC magnetic alloy systems.

3.1 RCo/Sm–Co-based magnets

As the second generation of rare-earth permanent magnets, Sm–Co-based magnets have been available since the early 1970s. The most interesting features of these magnets are high-energy products (14–30 MGOe), reliable coercive force, and the best temperature characteristics in the family of rare-earth materials.

Sm–Co-based magnets not only have better corrosion and oxidation resistance but also exhibit better temperature stability. This is the ideal material in applications such as pump couplings, sensors, and servomotors [63]. Two kinds of Sm–Co magnets are available in the market: (1) sintered magnets and (2) bonded magnets. The sintered magnets are formed through the powder metallurgy route as discussed earlier. In bonded magnets, thermoelastomer and thermoplastic resins are blended together with a variety of magnetic powders. The Sm–Co system forms two related equilibrium phases in Co-rich compositions [64]: (1) the CaCu₅-type SmCo₅ structure and (2) the Th₂Zn₁₇- or Th₂Ni₁₇-type Sm₂Co₁₇ structure. The Sm₂Co₁₇ structure is related to the SmCo₅ structure through the ordered substitution of one Sm by a pair of Co atoms (commonly referred to as Co dumbbells) (Equation 8).



In addition to the ordered Sm₂Co₁₇ dumbbell structures, the dumbbell arrangement can be randomized on the rare-earth sites as the disordered TbCu₇-type structure [64]. This metastable structure has the same unit cell as the CaCu₅ structure. The different crystal structures of the Sm–Co alloy system have been shown in **Figure 16**.

The suppression of the long-range order, leading to the formation of the TbCu₇-type SmCo₇ structure, has been accomplished by melt spinning [65], splat cooling [66], mechanical alloying [67], and some other special processes [68–70]. The formation of the disordered SmCo₇ structure has provided pathways to the development of materials with novel structures, as exemplified by recent advancements in the elevated-temperature performance of Sm–Co-based materials.

The microstructure and the magnetic properties obtained are strongly dependent on the alloy composition, processing parameters, and heat treatments. The melt-spun ribbons produced by rapid solidification exhibited higher intrinsic properties, improved microstructures, and better magnetic properties ($M_r \sim 8.5$ kG, $H_c \sim 4.1$ kOe, $(\text{BH})_{\text{max}} \sim 18.2$ MGOe, and a high remanence ratio of 0.9) [18]. Zr and Cu substitution for Co helped to reduce the crystallographic texture, and Sm(Co_{0.74}Fe_{0.1}Zr_{0.04}Cu_{0.12})_{8.5} ribbons were nearly isotropic [19]. In magnetically anisotropic SmCo₅ ribbons, well-crystallized

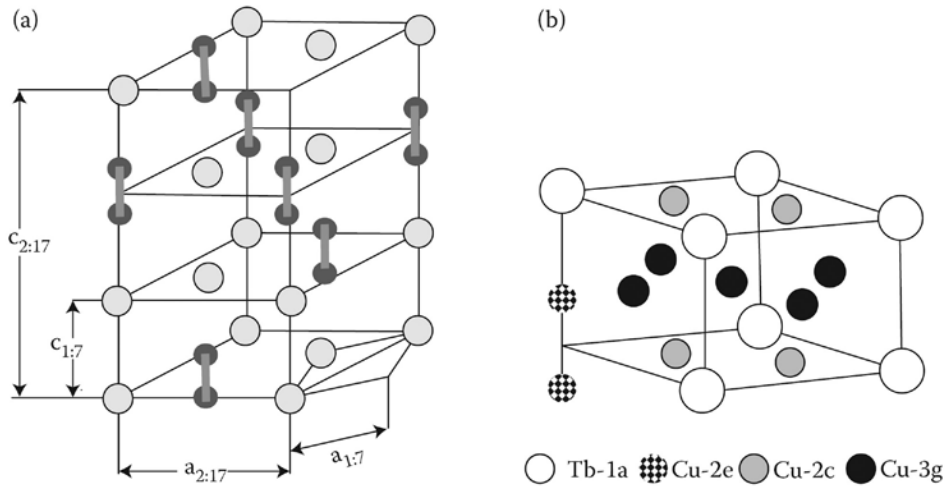


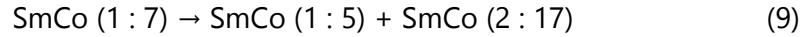
Figure 16. (a) Schematic showing Sm (●) and Co (●) dumbbell atoms. (Adapted from S. Aich, Crystal structure, microstructure and magnetic properties of SmCo-based permanent magnets, PhD dissertation, University of Nebraska, Lincoln, NE, 2005.) (b) Schematic diagram of hexagonal TbCu₇ crystal structure. (Reprinted with permission from J. Luo et al., *Intermetallics* 13, 2005, 710–716.)

grains with hexagonal structure (P6/mmm) were observed. Due to the addition of Fe in SmCo₅Fe_x ($x = 0, 1, \text{ and } 2$) melt-spun ribbons, produced by using a wheel speed of 25 m/s, the highest magnetic properties were observed for $x = 2$ ribbons due to their lowest content of Sm-rich phase and the smallest grain size [20]. Due to higher surface-to-volume ratio for $x = 2$, the intergrain exchange coupling enhanced the remanence. Improved magnetic properties (coercivity as high as 38.5 kOe) were reported for the melt-spun Sm(Co_{0.74-x}Fe_{0.1}Cu_{0.12}Zr_{0.04}B_x)_{7.5} ($x = 0.005\text{--}0.05$) alloys [21]. Better magnetic properties were reported for the boron-containing samples than the carbon-containing samples in melt-spun Sm(CoFeCuZr)₂M_x ($M = \text{B or C}$) nanocomposite magnets due to the finer grain size (30–50 nm) of the former [22].

3.1.1 Addition of alloying elements/stabilizing (1:7) phase

Stabilizing the 1:7 phase with TbCu₇ structure, which was first discovered by Buschow and van der Goot [71], is an important and challenging aspect to consider during synthesizing Sm–Co binary compounds. The growing interest to stabilize the 1:7 phase can be attributed to the achievement of the combined merits of SmCo₅ (strong magnetic anisotropy) and Sm₂Co₁₇ (large saturation magnetization and high Curie temperature). The Sm–Co 1:7 compound is usually prepared by milling, melt spinning, and mechanical alloying followed by a suitable heat-treatment schedule to crystallize the amorphous

1:7 phase. But, annealing results in decomposition of the Sm–Co 1:7 phase into 1:5 and 2:17 phases. The decomposition of SmCo_7 is attributed to the higher enthalpy of formation compared to its neighbor SmCo_5 .



Therefore, interest has been grown to focus on the addition of third element to synthesize the $\text{Sm}(\text{Co},\text{M})_7$ compound with TbCu_7 structure (space group $P6/mmm$) to use them as potential high-temperature rare-earth permanent magnets [67,69,72,73]. The feasibility of $\text{Sm}(\text{Co},\text{M})_7$ compound formation depends on several factors such as

- Enthalpy of formation of MCo_7
- Atomic radius ratio of Sm to (Co,M)
- Electronic configuration of M (the doping element)

While the magnetic properties of $\text{Sm}(\text{Co},\text{M})_7$ compounds depend on the site occupation of the stabilizing element M, which can be determined by the two factors:

- Enthalpies of solution of M in liquid Sm and Co
- Electronegativity difference in M, Sm, and Co

3.1.1.1 Electronegativity and site occupancy of the doping elements

The 1:7 phase can be regarded as a derivative of CaCu_5 structure (space group $P6/mmm$), a disordered structure where the Co–Co “dumbbell” pairs are randomly substituted for the Sm atoms occupying the 1a sites (see **Figure 16**) [71]. In Figure 16a, $\text{Sm}_2\text{Co}_{17}$ is a rhombohedral ($R\bar{3}m$) $\text{Th}_2\text{Zn}_{17}$ -type structure. The relation between the lattice parameters for the two structures is

$$\begin{aligned} c_{2:17} &= 3c_{1:7} \\ a_{2:17} &= \sqrt{3}a_{1:7} \end{aligned} \quad (10)$$

The magnetic anisotropy field depends on the content (amount) and the site occupancy of the third element M. The site occupancy of M depends on its electronegativity. When the electronegativity of M is less than that of Co, M prefers to occupy the 2e crystal position, whereas for higher electronegativity of M (higher than Co), M tends to be at the 3g site. In **Table 3**, the electronegativity values and corresponding site occupancy for a few doping elements have been mentioned. The stabilizing elements Si and Cu prefer

Table 3. Electronegativity and Corresponding Site Occupancy for Some Doping Elements

| <i>Element</i> | <i>Electronegativity</i> | <i>Site Occupancy</i> |
|----------------|--------------------------|-----------------------|
| Cu | 1.75 | 3g |
| Si | 1.74 | 3g |
| Co | 1.70 | |
| Ti | 1.32 | 2e |
| Hf | 1.23 | 2e |
| Zr | 1.22 | 2e |

to occupy the 3g site because of their higher electronegativity than that of Co, whereas Ti, Zr, and Hf have preference to occupy the 2e as they have lower electronegativity than that of Co. Considering the content of M, for M greater than 3 (as in SmCo_3Cu_4), M prefers to occupy the 2c site (Figure 16) [74,75]. The anisotropy field of the SmCo compound with 1:7 phase increases if M occupies the 2e and 3g sites, but decreases if it occupies the 2c site.

3.1.1.2 Enthalpy of formation

Considering a binary alloy containing two kinds of atoms (A and B), the enthalpy of formation of binary transition-metal intermetallics can be estimated using Miedema's empirical formula [76–78]:

$$\Delta H^{\text{form}} = \frac{x_A V_A f_A^B \left[-P(\varphi_A - \varphi_B)^2 + Q \left\{ (n_{\text{ws}}^A)^{1/3} - (n_{\text{ws}}^B)^{1/3} \right\}^2 - R \right]}{\left\{ (n_{\text{ws}}^A)^{-1/3} + (n_{\text{ws}}^B)^{-1/3} \right\}} \quad (11)$$

where ΔH^{form} is enthalpy of formation; x_A is atomic concentration of element A in the binary alloy; V_A is atomic volume of atom A; f_A^B is the extent to which an A atom is in contact with its dissimilar atom B; φ_A and φ_B are the electronegativity of A and B atoms, respectively; n_{ws}^A and n_{ws}^B are electron density per Wanger–Seitz cell of A and B atoms, respectively; and P, Q, and R are constants for the given group of metals.

Theoretical calculations using Miedema's empirical formula mentioned above show that the enthalpy of formation of MCo_5 and MCo_7 (where M = Si, Ti, Zr, and Hf) is less than -16 and -12 kJ/mol, respectively. The experimental results match with the theoretical calculations and confirm that Si, Cu, Ti, Zr, and Hf can be used as effective stabilizing elements for $\text{Sm}(\text{Co},\text{M})_7$ compounds. According to theoretical calculations based on Miedema's formula, Al, Nb, and Ta can also be considered as the stabilizing elements as the enthalpy of formation of MCo_5 and MCo_7 satisfies the above requirement.

However, Al, Nb, and Ta cannot be used (relatively difficult to use) to stabilize the Sm–Co-based 1:7 phase due to their electronic configurations [74]. In the case of Cu, theoretically calculated enthalpy of formation of MCo_5 and MCo_7 ($M = Cu$) does not satisfy the requirement for stabilizing the 1:7 phase. However, the $Sm(Co,Cu)_7$ compounds exhibit different stabilizing mechanisms, which may be related to the large mutual solubility between Co and Cu in the $Sm(Co,Cu)_7$. In the Co-rich part of the $Sm(Co,Cu)_7$ compound, the compound with the $TbCu_7$ -type structure can be stabilized by Cu element, whereas in the Cu-rich part of the $Sm(Co,Cu)_7$ compound, the Sm–Cu-based 1:7 phase can be stabilized by Co element. Therefore, Co and Cu can have a large mutual solubility in the $Sm(Co,Cu)_7$ compound and the $SmCo_{7-x}Cu_x$ compound has a large homogeneity region with $0.8 \leq x \leq 4.0$ [73], which results in the different stabilizing mechanism of Cu.

3.1.1.3 Atomic radius of the doping element

To satisfy the geometrical requirement of forming the $Sm(Co,M)_7$ compound with the $TbCu_7$ -type structure, the atomic radius of the doping element M must be larger than that of Co. The amount of the doping element M required to stabilize $SmCo_{7-x}M_x$ compound is inversely proportional to the atomic radius of the doping element. Table 7.4 shows how the amount required of different doping elements depends on their atomic radii [74].

The ratio of the atomic radius of the alloy $SmCo_{7-x}M_x$ can be expressed as [76–78]

$$r_p = \frac{r_{Sm}}{r_{Co+M}} = \frac{7r_{Sm}}{(7-x)r_{Co} + xr_M} \quad (12)$$

where r_{Sm} and r_{Co+M} are the atomic radius of Sm and the weighted average of the atomic radius of Co and M, respectively, and x is the amount of M. From Equation 12, it is clear that the ratio of the atomic radius r_p is a function of the content of doping element M. The structural stability of $SmCo_{7-x}M_x$ compounds depends on the effective Sm/(Co,M) atomic radius ratio (r_p) and the difference in electronegativity (e_n) between Sm and (Co,M). Usually, the SmCo 1:7-type structure can be stabilized in the range from 1.08(5) to 1.12(9) for r_p and from $-1.04(4)$ to $-0.94(4)$ for e_n [75]. Another research group reported that the range of r_p should be considered from 1.421 to 1.436 for stabilizing the $SmCo_{7-x}M_x$ compounds, which is less than the atomic radius ratio of Sm to Co (1.44) [74].

The amount of doping (stabilizing) element also influences the magnetic properties of the $Sm(Co,M)_7$ compound. Both the saturation magnetization and Curie temperature of $Sm(Co,M)_7$ compounds decrease with increasing

Table 4. Dependence of Atomic Radius on the Amount Required of the Doping Elements

| <i>Doping Element</i> | <i>Atomic Radius (Å)</i> | <i>Amount Required (x)</i> |
|-----------------------|--------------------------|----------------------------|
| Zr | 1.60 | 0.19 |
| Hf | 1.58 | 0.21 |
| Ti | 1.46 | 0.30 |
| Si | 1.34 | 0.90 |

M content, while the magnetic anisotropy increases with increasing M content. The Curie temperature decreases almost linearly with the increase in M content since the doping of nonmagnetic stabilizing element weakens the exchange interaction between the Sm and Co sublattices. A remarkable large reduction in Curie temperature ($T_c = 445^\circ\text{C}$) in the case of Si doping compared to other doping elements is attributed to its ability to be present in large amount ($x = 0.9$) in $\text{Sm}(\text{Co},\text{M})_7$ compounds. The doping element Cu has the least effect on the Curie temperature of $\text{SmCo}_{7-x}\text{Cu}_x$ compounds, and the Curie temperature decreases from 850.8°C for $x = 0.8$ to 810.8°C for $x = 2.0$ [73].

Using Hf and Zr as the stabilizing elements helps not only to stabilize the 1:7 phase but also to increase the magnetic anisotropy field of the $\text{SmCo}_{7-x}\text{M}_x$ alloy as they (Zr and Hf) as third metallic elements prefer to occupy the 2e site [67,74,75,79]. However, due to the poor formation ability of amorphous Sm–Co [80], it is difficult to achieve the fine grain size distribution, which is highly desirable to achieve high hard magnetic performance in ribbons [81]. One research group has reported that a small addition of carbon is helpful for grain refinement [82].

3.1.2 Addition of C/B as a grain refiner

Aich et al. reported the rapidly solidified melt-spun ribbons (isotropic) of binary Sm–Co alloys, which can achieve better microstructures and improved magnetic properties when modified with Nb/Hf and C/B addition [17,83–85]. The addition of Nb/Hf and C/B helps to decrease the size of the Co precipitate (~ 10 nm), which helps to improve exchange interactions between hard phase and soft phase resulting in improved remanence values. The addition of Nb/Hf stabilizes the 1:7 phase, also reduces size of (1:7) Phase, and helps to improve coercivity. **Figure 17** represents some micrographs of $\text{SmCo}(\text{Nb}/\text{Hf})(\text{B}/\text{C})$ alloys obtained using high-resolution transmission electron microscope (JEOL2010). Without any alloying addition (Figure 17a), the microstructure shows micron-sized big grain with larger-sized

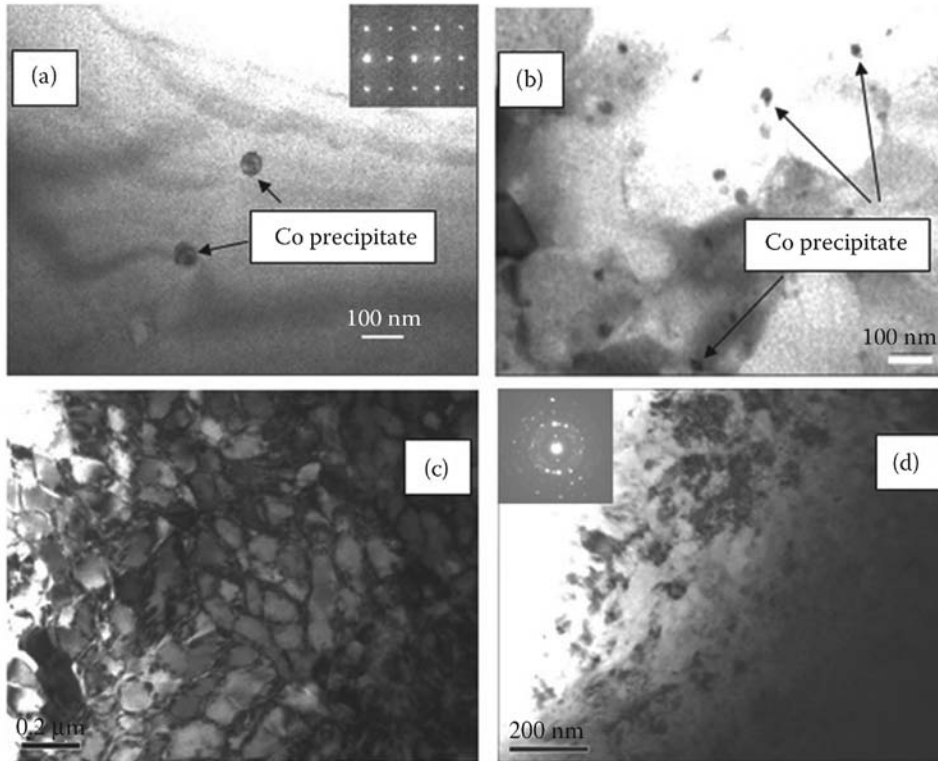


Figure 17. Bright-field TEM micrographs of $(\text{Sm}_{0.12}\text{Co}_{0.88})_{100-(x+y)}(\text{Nb/Hf})_x\text{C}_y$ alloys melt spun at 40 m/s; **(a)** $x = \text{Nb} = 0, y = \text{C} = 0$; **(b)** $x = \text{Nb} = 3, y = \text{C} = 0$; **(c)** $x = \text{Hf} = 3, y = \text{B} = 2$; and **(d)** $x = \text{Hf} = 3, y = \text{C} = 2$.

Co precipitates (~ 80 nm), whereas addition of Nb and C resulted in reduced size of (1:7) phase as well as smaller size of Co precipitates (~ 10 nm) (Figure 17b). The addition of Hf and C also helps to stabilize the 1:7 phase and results in grain refinement (Figure 17c). From Figure 17, it is clear that Hf and C/B addition results in more grain size reduction (nanograins) compared to the case of Nb and C addition.

Chang et al. [86,87] reported the microstructure, magnetic properties, and phase evolution of melt-spun $\text{SmCo}_{7-x}\text{Hf}_x\text{C}_y$ and $\text{SmCo}_{7-x}\text{Zr}_x\text{C}_y$ ($x = 0-0.4$; $y = 0$ and 0.1) ribbons. The phase transformation and microstructure of the ribbons with Hf substitution are similar to those with Zr. The ribbons with Hf substitution and a slight C addition exhibit a much higher coercivity and energy product than the Zr- and C-containing ribbons, because Hf substitution is more effective in increasing the anisotropy field of 1:7 phase than Zr substitution. The grain size distribution is almost unchanged with the element substitution. The Hf-substituted ribbons exhibited much higher coercivity and energy product compared to the Zr-substituted ribbons. For the alloys with $x = 0.4$, the maximum intrinsic coercivity (H_c) increases from 1.9 kOe for SmCo_7 ribbon to 17.2 kOe for $M = \text{Hf}$ and 11.0 kOe for $M = \text{Zr}$. Due

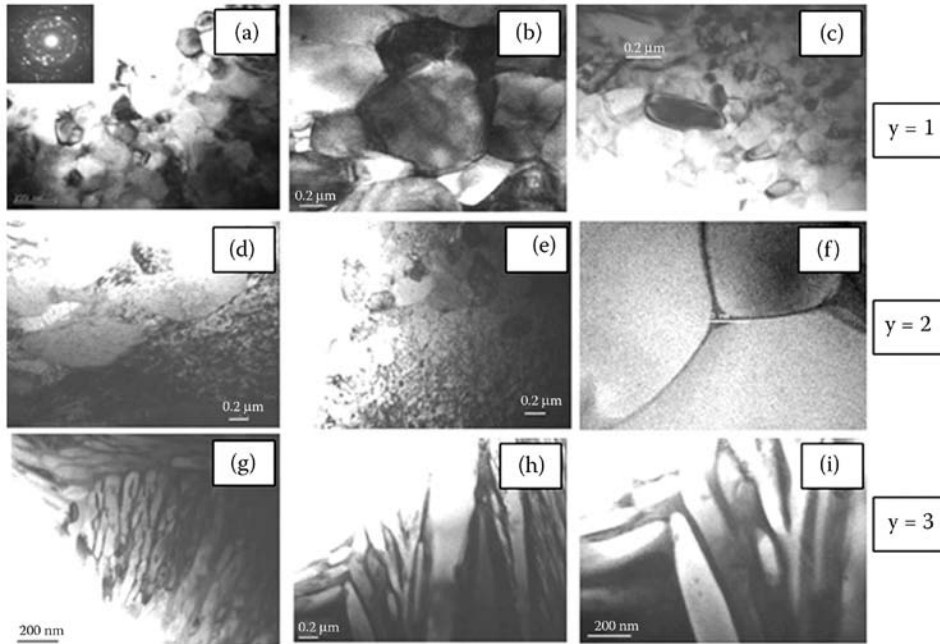


Figure 18. Transmission electron micrographs revealing the microstructure of the $(\text{Sm}_{12}\text{Co}_{88})_{100-y}\text{C}_y$ alloy melt spun at 40 m/s for $y = 1$, $y = 2$, and $y = 3$, showing morphological transition from equiaxed grains to dendritic structures; **(a–c)** for $y = 1$ showing equiaxed grains with a wide range of size distribution—**(a)** with an inset at the top left corner showing SAED pattern indicating the presence of nanocrystalline grains; **(d–f)** for $y = 3$ showing a mixture of smaller and larger equiaxed grains—**(f)** showing a triple point grain boundary; **(g–i)** for $y = 5$ showing dendritic microstructure—**(g)** very fine strangled dendritic structures, **(h)** a mixture of fine and coarse dendrites, and **(i)** relatively coarser dendritic structures.

to the addition of a small amount of C in both Hf- and Zr-substituted ribbons, grain refinement occurs and the fcc-Co phase with a grain size of 5–10 nm appears, which results in a stronger exchange coupling effect between the grains leading to achievement of further improved magnetic properties. The optimal magnetic properties of $B_r = 6.8$ kG, $iH_c = 11.7$ kOe, and $(\text{BH})_{\text{max}} = 10.4$ MGOe have been achieved in $\text{SmCo}_{6.8}\text{Hf}_{0.2}\text{C}_{0.1}$ ribbons due to the larger volume fraction of Co phase and the stronger intergranular exchange coupling effect.

The addition of carbon resulted in not only the grain refinement (from micron scale to nanoscale) but also the morphological changes in the microstructures [17,88]. At lower percentage of carbon addition ($y = 1$), equiaxed grains with a wide range of grain sizes (~ 100 – 700 nm) were observed (**Figure 18a–c**), with micron scale grains in a few regions. The electron beam diffraction pattern is shown in the inset of **Figure 18a**, indicating the formation of the nanocrystalline structure.

Figure 18d–f shows the microstructure for $y = 3$, which reveals a wide distribution of grain sizes. Figure 18d shows large elongated leaf-like structures embedded in a matrix of tiny substructures. In Figure 18e, small equiaxed grains, again embedded in a matrix of tiny substructures, were observed. The substructure contrast is caused by disorder (strain). Figure 18f represents a triple point grain boundary. At a higher percentage of carbon addition ($y = 5$), the microstructural morphology changes from equiaxed grains to dendrites, with the dendritic structure on the order of 150 nm long and 50 nm wide with a few coarse dendrites in some regions (Figure 18g–i). In Figure 18g–i, we can see dendritic microstructures exhibiting the presence of various sizes of dendrites. In Figure 18g, we see strangled fine dendritic structures. In Figure 18i, some relatively coarser dendrites are present and in Figure 18h, a mixture of coarse and fine dendrites are present with a few very coarse dendrites ($\sim 2.0 \mu\text{m}$ long and $\sim 0.45 \mu\text{m}$ wide).

The coercivity was found to vary linear with x (%Co), ranging from 17.5 kOe at $x = 0.67$ to 2.75 kOe at $x = 3$ in $\text{Sm}_{1/(1+x)}\text{Co}_{(5+x)/(6+x)}\text{Nb}_3\text{C}_3$ alloys (**Figure 19**) [17]. The change in coercivity (H_c) was associated with a decrease in magnetocrystalline anisotropy (K_1) as x increased. Equation 13 describes the relation between the coercivity and the anisotropy

$$H_c = \frac{2\alpha K_1}{\mu_0 M_s} - NM_s \quad (13)$$

where N is the demagnetization factor, M_s is the saturation magnetization, and μ_0 and α are the permeability and the microstructural parameter,

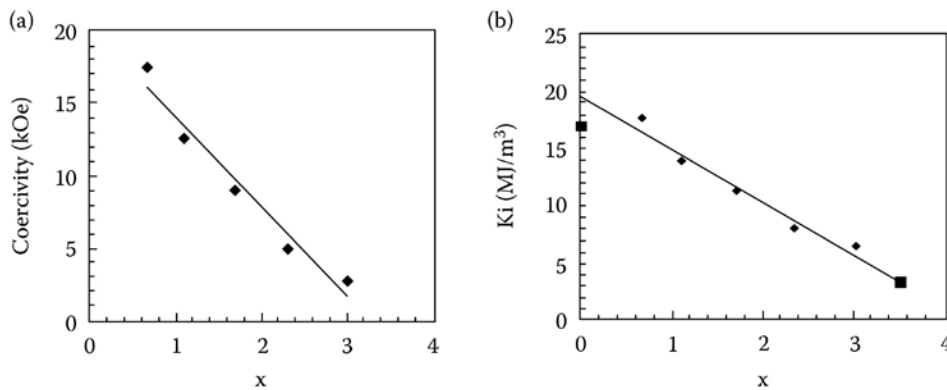


Figure 19. (a) Relationship between composition (x) and intrinsic coercivity for the $\text{Sm}_{1/(1+x)}\text{Co}_{(5+x)/(6+x)}\text{Nb}_3\text{C}_3$ alloys. (From S. Aich, Crystal structure, microstructure and magnetic properties of SmCo-based permanent magnets, PhD dissertation, University of Nebraska, Lincoln, NE, 2005.) (b) Relationship between composition (x) and the magnetocrystalline anisotropy of the $\text{Sm}_{1/(1+x)}\text{Co}_{(5+x)/(6+x)}\text{Nb}_3\text{C}_3$ alloys. The square end points denote the literature values for the SmCo_5 ($x = 0$) and $\text{Sm}_2\text{Co}_{17}$ ($x = 3.5$) compounds.

respectively. Consequently, it appears that the intrinsic magnetism depends more on the concentration of transition-metal dumbbells than their ordering on the lattice.

3.1.3 Effect of wheel speed and heat treatment

Wheel speed also influences the microstructure and the magnetic properties of the rapidly solidified Sm–Co alloys (**Figure 20**). Higher wheel speed raises the chances of nonequilibrium cooling, which is directly related to the chances of formation of Co precipitates. Also at higher wheel speed, reduced size of Co precipitates helps to improve the remanence and smaller 1:7 grain results in better coercivity.

Heat treatments were accomplished on the selected samples at temperatures ranging from 700°C to 900°C for 15 minutes. The ribbons were first wrapped in tantalum foil and then were sealed in quartz capsules in the presence of argon. The quartz capsules were then heat-treated in a tube furnace according to the heat-treatment schedule mentioned above followed by water quenching. The heat-treated samples showed order–disorder transformations. The order–disorder transformations during heat treatment in Sm–Co alloys can be expressed as



where R stands for Sm atoms and $r = 1/3$.

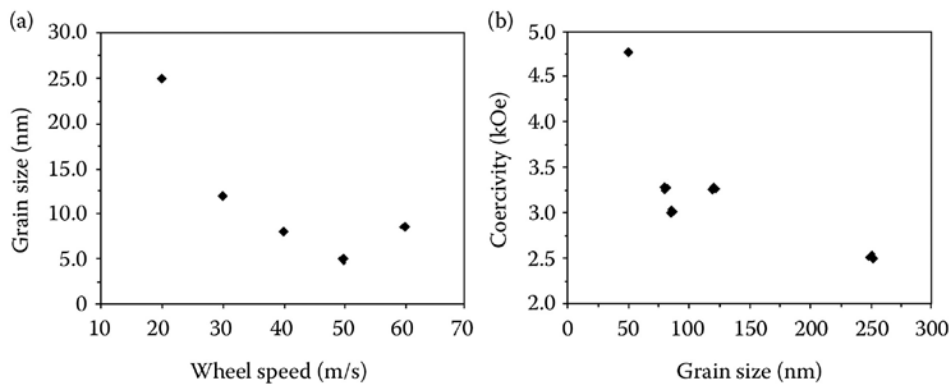


Figure 20. (a) Relationship between the grain size and the wheel speed of the $Sm_{11}Co_{89}$ –NbC alloys. (From S. Aich, Crystal structure, microstructure and magnetic properties of SmCo-based permanent magnets, PhD dissertation, University of Nebraska, Lincoln, NE, 2005.) (b) Relationship between the grain size and the coercivity of the $Sm_{11}Co_{89}$ –NbC alloys. (From S. Aich, Crystal structure, microstructure and magnetic properties of SmCo-based permanent magnets, PhD dissertation, University of Nebraska, Lincoln, NE, 2005.)

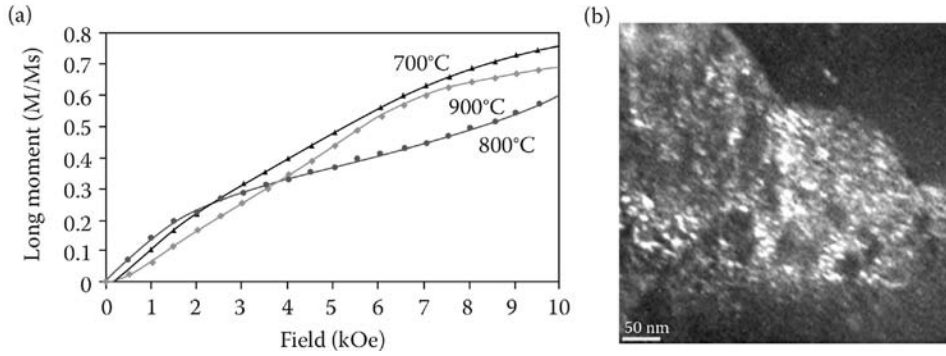


Figure 21. (a) Magnetization behavior of $(\text{Sm}_{12}\text{Co}_{88})\text{NbC}$ alloy annealed at 700°C, 800°C, and 900°C. (b) Dark-field image of transmission electron micrographs revealing the microstructures of $\text{Sm}_{12}\text{Co}_{88}$ alloy melt spun at 40 m/s and annealed at 800°C.

The transformation from the disordered TbCu_7 -type SmCo_7 structure to the ordered $\text{Th}_2\text{Zn}_{17}$ -type $\text{Sm}_2\text{Co}_{17}$ structure was found to greatly influence the magnetic behavior of the Sm–Co-based alloys. Transition from nucleation-dominated magnetization to pinning-dominated magnetization was observed (**Figure 21a**). The magnetic behavior suggests that anti-phase boundaries that developed during the ordering process acted as pinning centers. The bright regions in Figure 21b indicate presence of ordered regions correspond to the anti-phase domains (APDs) which provided significant interface area (anti-phase boundaries [APBs]) that acted as domain wall pinning sites.

3.1.4 Rare-earth magnets as high-temperature magnets

Sm–Co alloys are candidates for high-temperature applications (in the fields such as aeronautics, space, and electronic cars), as they exhibit excellent magnetic properties at ambient temperature, such as large magnetocrystalline anisotropy field (6–30 T), high Curie temperature (720–920°C), and large energy product ($>200 \text{ kJ/m}^3$) [89]. However, the highest service temperature of commercial 2:17-type Sm–Co magnets is only 300°C, and many efforts have been devoted to develop novel high-temperature permanent magnets, namely, development of high-temperature 2:17-type Sm–Co magnets, nanocrystalline Sm–Co magnets, and nanocomposite Sm–Co magnets.

The 2:17-type Sm–Co magnets are now available for application at 500°C or higher in the field of aeronautics and space limited by the cost. If the cost of the magnets can be lower, then the application will spread rapidly into the field of new energy, such as in electronic cars and wind turbines. The magnetic performance of the magnets is sensitive to the composition and heat treatment. Compared with traditional 2:17-type Sm–Co magnets,

the high-temperature 2:17-type Sm–Co magnets have less Fe, higher Sm, a cellular structure with smaller size, and a much finer domain structure. The enhancement of coercivity of the magnets during the slow cooling process mainly correlates with the Cu concentration and gradient in the 1:5 phase or the increase of anisotropy of the 1:5 phase.

Both the nanocrystalline Sm–Co magnets and nanocomposite Sm–Co magnets have potential for high-temperature applications. The main problem of these two kinds of magnets is that the magnetic performance of the magnets is relatively low because it is hard to obtain high texture degree in the magnets. Many efforts have been devoted to prepare anisotropic magnets, and magnets with a certain degree texture have been produced by methods of hot compaction plus hot deformation, surfactant-assisted ball milling plus spark plasma sintering, directional annealing, and so on. However, the preparations of anisotropic bulk nanocrystalline Sm–Co magnets and nanocomposite Sm–Co magnets with high texture degree are still big challenges and need further research. If this problem can be solved, then the nanocrystalline Sm–Co magnets and nanocomposite Sm–Co magnets may surpass the 2:17-type Sm–Co magnets and become the new-generation high-temperature permanent magnets. And the improvement of the magnetic properties will speed the applications in the market.

3.1.5 Oxidation protection for Sm–Co magnets

During the operation of high-temperature permanent magnets, undesirable oxidation at high temperatures is a major issue for potential applications [89]. Two approaches—(1) alloying [90,91] and (2) surface modification [92,93]—were considered as the effective ways to protect rare-earth magnets at high temperature by increasing their oxidation resistance. Alloying nonmagnetic element Si can effectively improve the oxidation resistance of Sm–Co magnets. Using the Sm–Co magnets at high temperature (as high as 500°C) for long time (~500 hours) creates much thinner internal oxidation layer (IOL) ~3–4 μm if Si is added in the magnets compared to the magnets without any Si addition (IOL ~ 212 μm). Also the loss of energy product for Si addition is much less (~5%–6%) compared to the magnets without any Si addition (~52%–53%). Moreover, Liu et al. reported that formation of SiO₂ as the IOL reduces the oxidation rate and oxygen diffusion coefficient, which effectively enhances the oxidation resistance in SmCo_{6.1}Si_{0.9} nanocrystalline magnets [90,91]. Although Si addition enhances the oxidation resistance in Sm–Co magnets, it deteriorates the magnetic properties of the magnets because of its nonmagnetic nature. Therefore, surface modification can be considered as the better way to protect the Sm–Co magnets from oxidation and has little effect on the magnetic properties at the same time. For instance, Ni-coated magnets show better stability (oxidation

resistant) at 500°C than uncoated magnets [92,93]. For an uncoated magnet treated at 500°C for 500 hours, the $(BH)_{\max}$ loss was ~40%, whereas for the Ni-coated magnet, the $(BH)_{\max}$ loss was only ~4%. Also, the other magnetic properties (B_r and H_c) were much higher in the case of coated magnet than the uncoated one [92,93]. The reason behind the improvement of oxidation resistance and enhancement of the magnetic properties in the case of Ni-coated magnets can be attributed to the low oxygen invasion and less Sm vaporization compared to the uncoated magnet. Also, research reveals that at different operation temperatures, different types of coating have the best performance. For example, some coatings such as diffused Pt coating and paint-like overlay coating containing titanium and magnesium oxides can show the best performance at 450°C as well as at 550°C [94]. Other examples are that sputtered SiO_2 is more effective at 450°C but less effective at 550°C, whereas alumina-based overlay coating is more effective at 550°C but less effective at 450°C.

For the high-temperature permanent magnetic materials, a new research direction may be the rare-earth-free magnetic materials that do not rely on the limited supply of rare-earth metals and cost less. Further research is needed to bring the new rare-earth-free magnetic materials for high-temperature applications, and computation methods of combinational materials science may be helpful for the progress.

3.2 R–Fe–B-based magnets/Nd–Fe–B-based magnets

In the R–Fe–B magnets group, Nd–Fe–B magnets are considered as the most demanding and challenging material. In spite of the recent discovery, the Nd–Fe–B magnets are considered as very important magnetic materials in permanent magnet industries because of their enhanced coercivity and large energy product, sometimes significantly higher than the Sm–Co magnets (as mentioned in Table 1 and Figure 4). The excellent magnetic behavior of the Nd–Fe–B magnet can be attributed to the combined effect of the large spontaneous magnetization of 3d metals and the strong anisotropy fields of rare-earth transition-metal compounds, and at the same time, the magnets maintain a high value of the Curie temperature [95]. These attractive magnetic properties made the Nd–Fe–B magnets appropriate to be used as the powder products for the bonded magnet applications and the fully intermetallic magnets having energy product significantly higher than the best Sm–Co-based magnets. The attractive magnetic properties are attributed to the presence of $\text{Nd}_2\text{Fe}_{14}\text{B}$ phase. Also, Nd–Fe–B magnets attracted much more attention because of their lower cost due to greater availability of Nd and Fe compared to the same of Sm and Co. The following sections describe different categories of Nd–Fe–B magnets, various processing routes for those magnets, and their properties and applications.

The Nd–Fe–B magnets are mainly categorized as (1) sintered magnets and (2) bonded magnets. They are described in detail in the following.

3.2.1 Sintered magnets

Sintered magnets or metallic magnets are produced by conventional casting and powder metallurgy route or hot deformation. Here, in this chapter, the discussion on metallic magnets has limited scope. So, our discussion is limited to bonded magnets.

3.2.2 Bonded magnets

Bonded magnets are also produced by powder metallurgy routes, but here a binder is used to “glue” the powder particles together. The powder is produced by rapid solidification technique. $\text{Nd}_2\text{Fe}_{14}\text{B}$ stoichiometric ribbons are produced by melt spinning followed by milling to produce powders. The powders are then bonded using thermal-set or thermal-plastic polymers followed by compression. The powder magnetic properties, loading factor, and molding technique influence the BH_{max} of the magnets. Powder should have high BH_{max} to get a high BH_{max} compact. High loading factor within molding capability of the alloy is essential to achieve a high BH_{max} magnet. Thermal properties of the powder and the molding polymer should be good to produce a high BH_{max} magnet [23]. The thermal stability of a polymer-bonded magnet depends on several factors, such as particle–particle interaction, binder–particle interaction, amount of binder, and density of the magnet. These factors are needed to be optimized in a potential aggressive environment [23]. Bonded magnets have the several advantages over the sintered magnets, such as [27]

- Easily accomplished near-net-shape processing
- Avoidance of eddy currents
- Good mechanical properties

The main disadvantage of bonded magnet is the dilution of magnetic properties due to the polymer binder [27]. Typical values of B_r and H_{ci} of various metallic and bonded magnets are shown in **Figure 22**. The properties of bonded NdFeB magnets lie between metallic Nd–Fe–B and ferrites.

Table 5 compares the magnetic properties of metallic (sintered and hot pressed) and bonded Nd–Fe–B magnets. Four important magnetic properties—intrinsic coercivity (H_c), remanence (B_r), maximum energy product $(\text{BH})_{\text{max}}$, and Curie temperature (T_c)—have been compared for those magnets.

For producing bonded magnets, injection molding is a more favorable technique than compression because of its low cost of processing [96]. Other

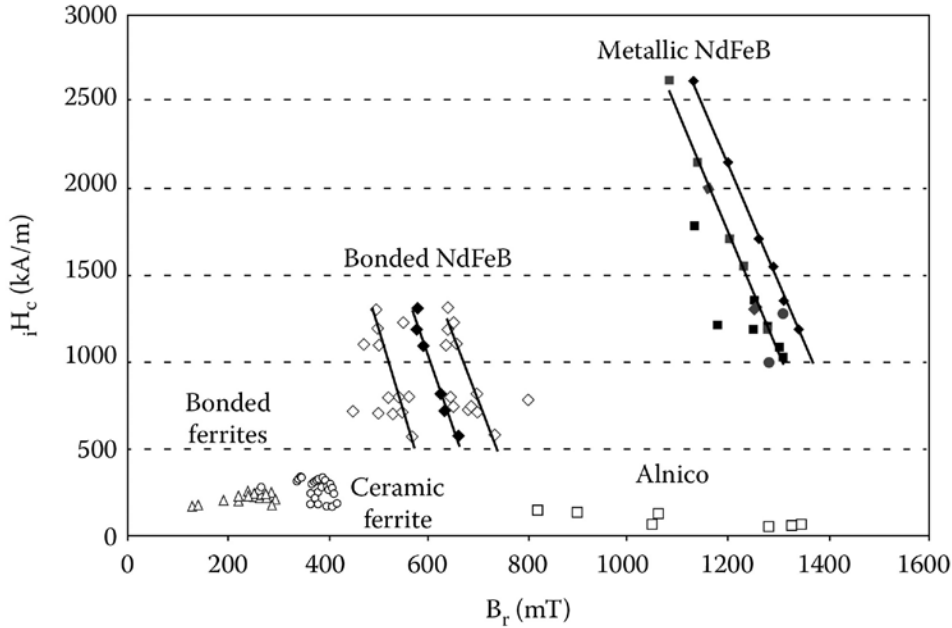


Figure 22. The B_r and iH_c plot of commercially available permanent magnets. (Reprinted with permission from B. M. Ma et al., *J. Magn. Magn. Mater.* 239, 2002, 418–423.)

Table 5. Magnetic Properties of Sintered and Bonded NdFeB Magnets

| Magnetic Property | Bonded Magnets | Metallic Magnets (Hot Pressed) | Metallic Magnets (Sintered) |
|-----------------------------------|----------------|--------------------------------|-----------------------------|
| iH_c (kA/m) | >720 | 1280–1400 | 1035–2600 |
| B_r (mT) | 690 | 820–1310 | 1080–1370 |
| $(BH)_{max}$ (kJ/m ³) | 80 | 130–340 | 220–360 |
| T_c (°C) | 360 | 335–370 | 310 |

techniques such as extrusion and calendaring are also used to produce bonded magnets, especially to produce flexible magnets. Magnets produced by calendaring are highly flexible and can be formed to any shape as required in the application. Also, calendaring is the cheapest process compared to the other processes mentioned above. But, as the loading factor is less for calendaring, the B_r and $(BH)_{max}$ values obtained by this process is less compared to other processes (compression, injection, and extrusion). To design a permanent magnet, the three important factors—*intrinsic coercivity* iH_c , *remanence* B_r , and *maximum energy product* $(BH)_{max}$ along with the temperature characteristics—should be considered other than the molding technique to achieve the desirable properties of the magnet. Powders produced by gas atomization have higher loading factor than those produced

by melt spinning because of the spherical morphology of the achieved atomized powder. Spherical powder always shows better flow ability during injection molding compared to other melt-spun powder, as the shear viscosity is much less in the case of spherical powder. The magnetic powders are mainly used in the automotive sector that needs high B_r , high H_c (>960 kA/m even at room temperature), and low flux aging loss when exposed to an elevated temperature. In **Table 6**, the loading factor, the flux aging loss, and the various magnetic properties are compared for a series of magnetic powder produced by Magnequench. Here MQP-B and MQP-13-9 are powders produced from melt-spun ribbons and MQP-S-9-8 is the spherical powders of NdFeB magnetic powder having bimodal distribution produced by inert gas atomization [96]. Among those three categories, when they are exposed to 180°C temperature for 100 hours, MQP-S-9-8 has the least flux aging loss compared to the other two (**Figure 23**). MQP-B has exhibited the maximum flux aging loss (as high as $\sim 15\%$) in the same condition [96].

Table 6. Loading Factors, Flux Aging Loss, and Magnetic Properties of MQP-B, MQP-13-9 (Injection Molded), and MQP-S-9-8 (Gas Atomized) Powders

| Magnet Powder | Loading Factor (vol.%) | Flux Aging Loss | B_r (mT) | $(BH)_{max}$ (kJ/m ³) | H_c (kA/m) |
|---------------|------------------------|-----------------|------------|-----------------------------------|--------------|
| MQP-B | 62 | Maximum | 540 | 85 | 720 |
| MQP-13-9 | 62 | Intermediate | 500 | 76 | 700 |
| MQP-S-9-8 | 69 | Minimum | 500 | 73 | 700 |

Source: Reprinted with permission from B. M. Ma et al., *J. Magn. Magn. Mater.* 239, 2002, 418–423.

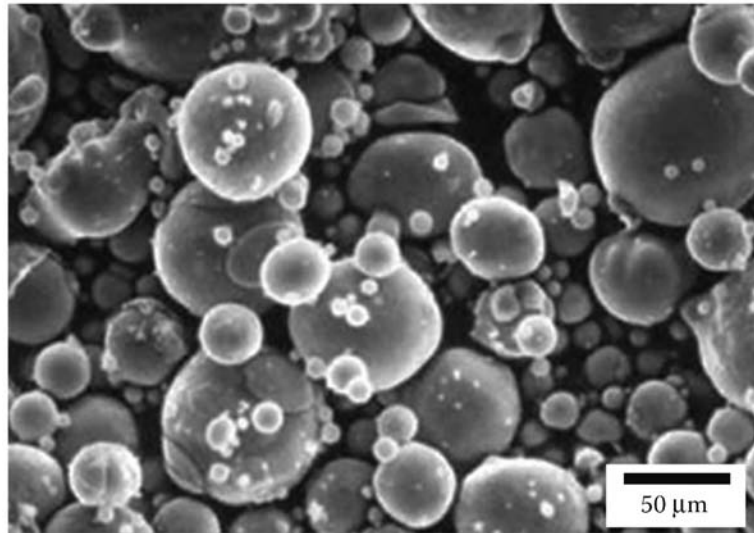


Figure 23. Morphology of MQP-S-9-8 powder. (Reprinted with permission from B. M. Ma et al., *J. Magn. Magn. Mater.* 239, 2002, 418–423.)

Spherical shape of the powder is important as production rate of powder is high, but cost of the powder is low, and mechanical strength of thin dimension magnet obtained is more in the case of spherical shaped powder compared to the same obtained from the other conventional processes [96].

Again, depending on the microstructure or grain size, the Nd–Fe–B magnets can be categorized as (1) nanocrystalline magnets and (2) microcrystalline magnets [23]. The microcrystalline magnets are produced by sintering the cast ingot (with relatively high rare-earth content ~ 15 at.%) using the conventional powder metallurgy route. At first, the cast ingot is pulverized using course grinder and then jet-miller to produce fine-powder particles ($\sim 5 \mu\text{m}$). Then the powder particles are aligned in a magnetic field (10–20 kOe) followed by pressing into a dense compact. Finally, sintering is done at $\sim 1100^\circ\text{C}$ for several hours followed by a post-sintering heat treatment at 600°C to relieve the internal stresses [23]. It is beyond our scope to discuss this aspect here in more detail. So, we are focusing on nanocrystalline magnets.

3.2.3 Nanocrystalline permanent magnets

The nanocrystalline Nd–Fe–B magnets can be produced by melt spinning to achieve the spun ribbon composition close to 2:14:1 [23]. The ribbons then subsequently are crushed into powder and either bonded with polymer to get bonded magnet or hot deformed to get fully dense magnet.

In any rare-earth transition-metal system, the magnetic properties mainly depend on the grain size or the presence/absence of the intergranular phases that influence the surface/interface effects that differ from the conventional bulk or microcrystalline magnets. Below a critical grain size, large coercivity can be obtained when the crystallite size reaches the single-domain region (**Figure 24**). In the single-domain region, the coercivity decreases for the ultrafine grains due to the thermal effects and the

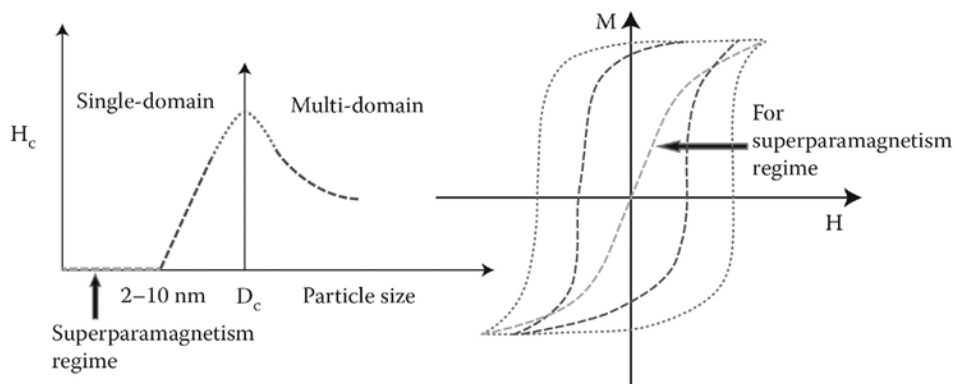


Figure 24. Magnetic properties of nanostructured materials.

coercivity eventually reaches to zero value in the superparamagnetism particle size regime (2–10 nm). Usually, in rare-earth transition-metal compounds, the critical size for single-domain particle is a fraction of a micron ($\sim 10^{-3}$ – 10^{-2} nm) [97].

Nanocrystalline magnets can be obtained not only by rapid quenching (melt spinning) but also by mechanical alloying, high-energy ball milling, and hydrogen-assisted methods, such as reactive/intensive milling and HDDR process [27]. But, all the methods produce isotropic magnets with randomly oriented grain structure having poor remanence and magnetic energy density $(BH)_{\max}$ compared to the ideal microstructure having some anisotropy with single-domain grain. Attempts have been made to maximize the energy density $(BH)_{\max}$ by hot deformation or inducing texture/anisotropy by anisotropic HDDR and to improve the remanence by exchange coupling [27].

The rapidly solidified Nd–Fe–B magnets (melt-spun ribbons) are usually isotropic in nature because of their random orientation of the grains resulting in poor magnetic properties (remanence and energy product). Better magnetic properties can be achieved for this isotropic ribbon when the ribbons are crushed and hot pressed to full density and finally are crushed after hot deforming the compact [7]. Although this is a complicated process, it results in anisotropic magnet powder, which can provide aligned Nd–Fe–B-bonded magnets having energy product as high as 145 kJ/m^3 [7]. Similarly, Pr–Fe–B-based magnets can also be produced by rapid quenching (melt spinning) [98,99], which have significant potential for low-temperature applications as they show no spin reorientation down to 4.2 K (which occurs at 135 K for $\text{Nd}_2\text{Fe}_{14}\text{B}$). Also, the Pr–Fe–B magnets are used to produce hot-deformed (textured) magnets.

Consolidation (by conventional polymer bonding or hot pressing) of rapidly solidified Nd–Fe–B melt-spun ribbons were associated with a uniform and fine crystalline (<100 nm diameter) microstructure primarily based on $\text{Nd}_2\text{Fe}_{14}\text{B}$ phase [100]. Anisotropic magnets produced by thermomechanical deformation of the consolidated isotropic Nd–Fe–B magnets can achieve the energy product as high as 45 MGOe [101]. Rapidly solidified (melt spinning) rare earth–transition metal–boron (RE–TM–B) alloys achieved better performance by modifying the compositions and by optimizing the microstructure [102].

Excellent magnetic properties of highly die-upset Nd–Fe–B magnets can be lowered by reduced coercivity and nonuniform deformation. Those limitations can be overcome by heat treatment, substitution, addition, and multistage die upsetting. After multistage (75%) die upsetting, the Nd–Fe–Co–B–Ga magnet was able to perform superior magnetic properties, having remanence and energy product as high as 14.5 kG and 48.5 MGOe, respectively [103].

3.2.4 Nanocomposite magnets

Nanocomposite magnets have been considered as high-performance magnets because of their superior energy products (higher than the conventional single-phase magnets), which is attributed to the exchange coupling between a hard magnetic phase with high coercivity and a soft magnetic phase with high saturation magnetization [104]. The $\text{Fe}_3\text{B}/\text{Nd}_2\text{Fe}_{14}\text{B}$ system is one of the good examples of nanocomposite magnets [105].

3.2.5 Protective coating to improve corrosion resistance

Nd–Fe–B magnets have poor corrosion resistance to humid environment [106]. The surface of the magnet should be coated with some protective coatings to protect the surface of the magnet from the aggressive environment.

Nd–Fe–B magnets can also be prepared using another well-known RSP technique named as high-pressure gas atomization (HPGA) [107]. In HPGA technique, rapid solidification of mixed rare earth–iron–boron alloys, $\text{MR}_2\text{Fe}_{14}\text{B}$ (MR = Nd, Y, Dy) magnet alloys, produced almost similar properties and structures as closely related alloys produced by melt spinning at low wheel speeds. Additions of titanium carbide and zirconium to the permanent magnet alloy design in HPGA powder (using He atomization gas) have made it possible to achieve highly refined microstructures with magnetic properties approaching melt-spun particulate at cooling rates of 10^5 – 10^6 K/s. By producing HPGA powders with the desirable qualities of melt-spun ribbon, the need for crushing ribbon was eliminated in bonded magnet fabrication. The spherical geometry of HPGA powders is more ideal for processing of bonded permanent magnets since higher loading fractions can be obtained during compression and injection molding. This increased volume loading of spherical magnet powder can be predicted to yield a higher maximum energy product $(\text{BH})_{\text{max}}$ for bonded magnets in high-performance applications.

Passivation of rare-earth-containing powder is warranted for the large-scale manufacturing of bonded magnets in applications with increased temperature and exposure to humidity.

Irreversible magnetic losses due to oxidation and corrosion of particulates is a known drawback of RE–Fe–B-based alloys during further processing, for example, injection molding, as well as during use as a bonded magnet. To counteract these effects, a modified gas atomization chamber allowed for a novel approach to *in situ* passivation of solidified particle surfaces through injection of a reactive gas, nitrogen trifluoride (NF_3). The ability to control surface chemistry during atomization processing of fine

spherical RE–Fe–B powders produced advantages over current processing methodologies. In particular, the capability to coat particles while “in flight” may eliminate the need for post-atomization treatment, otherwise a necessary step for oxidation and corrosion resistance. Stability of these thin films was attributed to the reduction of each RE’s respective oxide during processing; recognizing that fluoride compounds exhibit a slightly higher (negative) free-energy driving force for formation. Formation of RE-type fluorides on the surface was evidenced through x-ray photoelectron spectroscopy (XPS). Concurrent research with auger electron spectroscopy has been attempted to accurately quantify the depth of fluoride formation to grasp the extent of fluorination reactions with spherical and flake particulates. Gas fusion analysis on coated powders (dia. <45 μm) from an optimized experiment indicated an as-atomized oxygen concentration of 343 ppm, where typical, nonpassivated RE-atomized alloys exhibit an average of 1800 ppm oxygen. Thermogravimetric analysis (TGA) on the same powder revealed a decreased rate of oxidation at elevated temperatures up to 300°C, compared to similar uncoated powder.

University of Delaware attempted to make isotropic nanocomposite $\text{R}_2\text{Fe}_{14}\text{B}/\alpha\text{-Fe}$ melt-spun ribbons to achieve the maximum energy product $(\text{BH})_{\text{max}}$ greater than 20 MGOe [8]. Three alloy compositions— $\text{Pr}_9\text{Fe}_{85}\text{B}_6$, $\text{Pr}_5\text{Nd}_5\text{Fe}_{19}\text{Co}_5\text{B}_6$, and $\text{Pr}_9\text{Co}_5\text{Fe}_{80}\text{B}_6$ —were melt spun at a wheel speed of 18 m/s in a temperature range of 1300–1500°C. The obtained $(\text{BH})_{\text{max}}$ value was improved by optimizing the temperature of the melt used during the melt ejection onto the rotating wheel, which helped to result in a homogeneous nanophase structure. Use of an optimum ejection temperature of 1360°C was able to provide the highest value of the reduced remanence $M_r/M_s = 0.8$ and $(\text{BH})_{\text{max}} = 21$ MGOe.

3.3 Interstitially modified R_2Fe_{17} -based permanent magnets

The Sm–Fe compounds are not useful as permanent magnet materials (for their basal plane easy magnetization direction) unless nitrogen or carbon diffusion expands the crystal structure and produces $\text{Sm}_2\text{Fe}_{17}\text{M}_x$ ($\text{M} = \text{N}$ or C). Interstitial diffusion of nitrogen or carbon in $\text{Th}_2\text{Zn}_{17}$ -type rhombohedral R_2Fe_{17} structure dramatically changes its intrinsic magnetic properties by increasing the Curie temperature (T_c) and by enhancing the magnetocrystalline anisotropy. The Curie temperature increases due to lattice expansion. In the case of interstitial diffusion of nitrogen in $\text{Sm}_2\text{Fe}_{17}$ compound, due to 6% volume expansion, the Curie temperature was increased from 116°C to 476°C [7]. The increase in magnetocrystalline anisotropy of interstitially modified magnets is attributed to the change in crystalline electric field due to the presence of interstitial nitrogen or carbon atom in the large 9e sites

[108]. Based on the crystal field theory, the anisotropy constant (K_1) can be expressed as [109]

$$K_1 = \frac{3}{2} N_R \alpha_j \langle r^2 \rangle \langle O_{20} \rangle A_{20} \quad (15)$$

where N_R is the rare-earth concentration, α_j is the Stevens factor, $\langle r^2 \rangle$ is the expectation value of the square of 4f radius, A_{20} is the crystal field parameter, and $\langle O_{20} \rangle$ is the expectation value of $3J_z^2 - J(J + 1)$, where J is the total angular momentum of the rare-earth ions. Unlike the binary R_2Fe_{17} compound, the ternary $R_2Fe_{17}M_x$ ($0 \leq x \leq 3$) nitrides or carbides are considered promising materials for permanent magnets. The high magnetic anisotropy of the $Sm_2Fe_{17}M_x$ magnet can persist even at high temperature, which made it challenging as a promising material for high-temperature applications replacing the Sm–Co-type expensive magnet. Relatively to a lower extent, the $RFe_{12-x}T_x$ ($T = W, V, Ti, Mo, Si$) compounds are also considered as the interstitially modified permanent magnets. In the case of 2:17 and 1:12 compounds, the potential to be used as permanent magnets is attributed to their enhanced magnetic anisotropy rather than the improved Curie temperature [109]. The magnetic anisotropy is a strong function of the crystal field parameter A_{20} , as mentioned in the above equation. The interstitial atoms occupy the positions very close to the rare-earth atom [110,111], which results in significant changes in A_{20} values. Some NMR experiments were carried out with the help of ^{89}Y spin-echo NMR on the compounds before and after charging with interstitial atom C, N, and H [112]. The experimental data were used to study the Y hyperfine field in Y_2Fe_{17} compounds as a function of increasing occupancy of the interstitial sites by the C, N, and H atoms. A strong decrease in the Y hyperfine field in the case of nitrides and carbides indicates the strong bonding effect (bonding between the on-site valence electrons of R atoms and the valence electrons of interstitial atoms). This bonding effect primarily determines the A_{20} value. In the case of interstitial hydrides, the change in the Y hyperfine field was negligible, which indicates a moderate bonding effect. The strong bonding effect of nitrides and carbides and related change in the A_{20} value explain the strong magnetic anisotropy associated with the nitride and carbide compounds. The changes in A_{20} value due to the interstitial bonding are different for 2:17 and 1:12 compounds, as they have different atomic arrangement for the interstitial atoms, as shown in **Figure 25**. To estimate the A_{20} value (the electric-field gradient at the 4f site), a rare-earth Mössbauer spectroscopy (^{155}Gd Mössbauer spectroscopy) was used [111], and from the measurement data it was derived that the electric-field gradient at the nuclear site (V_{zz}) of R_2Fe_{17} compound was changed from 4.4×10^{21} to 16.2×10^{21} V/m² due to nitro- genation. In the case of 1:12 compound, the V_{zz} value was changed from 1.6×10^{21} to -21.3×10^{21} V/m² (enhancement of field gradient is accompanied

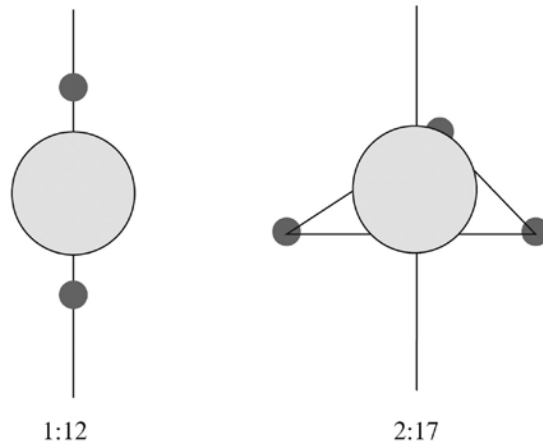
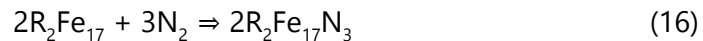


Figure 25. Different atomic arrangements for the interstitial atoms for 1:12 and 2:17 phases.

by a sign reversal) [112]. Usually, changes of similar magnitude and sign are expected for A_{20} . So, in the latter case, the enhancement of the field gradient accompanied by a sign reversal may be attributed to the different sign of α_j (Equation 15) of the R elements employed in 2:17 nitride compound (Sm) than in 1:12 nitride compound (Pr, Nd).

A simple gas-phase nitrogenation can be carried out according to the following reaction [7]:

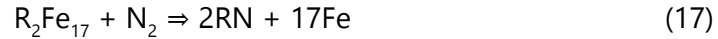


Temperature and pressure were maintained at ~ 1 bar and ~ 400 – 500°C , respectively. This type of gas–solid reaction takes place in three stages:

1. Adsorption of the gas molecules
2. Dissociation and subsequent chemisorption of the gas molecules
3. Long-range diffusion into the metal matrix

In the above nitrogenation process/reaction (Equation 16), the temperature should be high enough to overcome the activation barrier to initiate the adsorption of nitrogen atoms. However, a detailed investigation is needed to explore the efficiency of the irreversible nitrogenation process, whether, in a thermodynamic equilibrium, a solid solution of ternary nitrides with fully nitrated and nonnitrated layers are obtained as the diffusion of nitrogen atom is significantly slow into the matrix. To improve the rate of nitrogen diffusion into the matrix, people attempted to produce fine-powder particles of nitrogen using intensive milling [113] or HDDR technique [114],

which eventually can be used during nitrogenation. It is well known that dislocations, grain boundaries, and any other free surfaces are considered as the high diffusivity paths as the mean jump frequency of atoms at those locations is much higher than that of the same atoms in the lattice. Microcracks and microcrystals provide faster and easier diffusion paths, leading to shorter annealing times and lower annealing temperatures in any processing. However, at lower temperatures, the following reaction (decomposition in RN and Fe) is thermodynamically preferable:



However, due to the difficulty to achieve the long-range diffusion of the metal atoms at the lower temperatures and insufficient kinetics, the formation of metastable ternary nitrides are to some extent successful compared to the more stable binary nitride and metallic Fe. Due to this poor thermal stability, ternary nitrides have limited applications in metal- and polymer-bonded magnets. Addition of alloying elements, such as Al, Si, and Ga, can help to improve the thermal stability (or to increase the decomposition temperature) [115–117].

In general, carbides are considered to be more thermally stable than nitrides although the latter shows better magnetic properties. Usually, standard casting techniques are used to produce the ternary carbides $R_2Fe_{17}C_x$ ($x \leq 1.5$). Better magnetic properties can be achieved by increasing the C concentrations either by partial substitution of Fe by Ga in the cast materials or by exposing fine particles of the binary compound to hydrocarbon gases at elevated temperatures (see reviews by Skomski et al. [118] or Fuji and Sun [15]). To achieve highly coercive powders, the grain size should be very small (grain refinement) and some special processing routes have been discussed by Muller et al. [119]. **Figure 26** compares the demagnetization curves of $Sm_2Fe_{17}N_3$ and $Sm_2Fe_{15}Ga_2C_2$ compounds. The $Sm_2Fe_{17}N_3$ compounds were prepared by mechanical alloying of the binary compound and subsequent nitrogenation of the alloy powder annealed at 750°C, whereas $Sm_2Fe_{15}Ga_2C_2$ compounds were prepared by mechanical alloying of the melt-carburized compound followed by annealing at 800°C [120]. The alloy without any Ga addition shows higher remanence and higher coercivity compared to the alloy with Ga addition. Addition of nonmagnetic alloying element (Ga) results in the reduction in saturation magnetization and decrease in the anisotropy field of the $Sm_2Fe_{15}Ga_2C_2$ alloys, leading to lower remanence and lower coercivity in $Sm_2Fe_{15}Ga_2C_2$ compounds. However, the thermal stability of the $Sm_2Fe_{15}Ga_2C_2$ alloy was much improved compared to the $Sm_2Fe_{17}N_3$ compounds, which facilitated accessing/ using the hot-pressing processing route to obtain fully dense magnets.

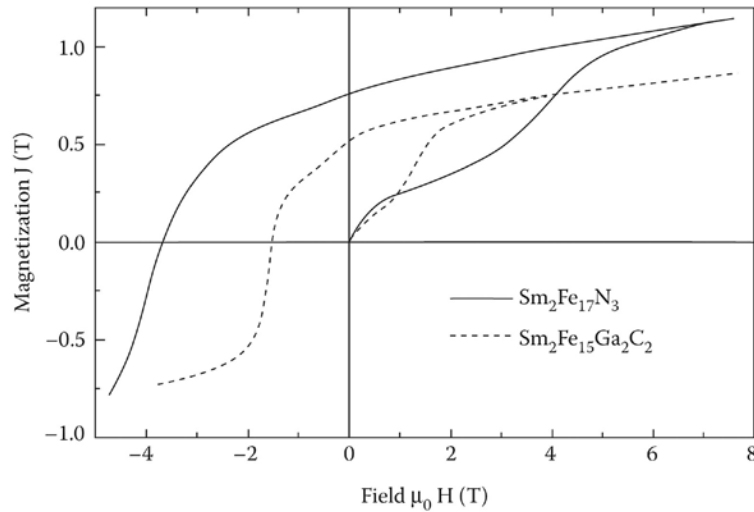


Figure 26. Comparison of demagnetization curves of $\text{Sm}_2\text{Fe}_{17}\text{N}_3$ prepared by mechanical alloying the binary compound and subsequent nitrogenation and annealing (750°C) and $\text{Sm}_2\text{Fe}_{15}\text{Ga}_2\text{C}_2$ prepared by mechanical alloying the melt-carburized compound followed by annealing at 800°C . (Reprinted with permission from O. Gutfleisch, *J. Phys. D Appl. Phys.* 33, 2000, R157–R172.)

Discovery of $\text{Sm}_2\text{Fe}_{17}$ -nitride has triggered a renewed interest in permanent magnets based on nitrides. $\text{Sm}_2\text{Fe}_{17}$ -nitride-based permanent magnets were produced by RSP (melt spinning with a linear velocity of 55 m/s), followed by annealing at 650°C for 10 minutes and subsequent nitrogenation at 450°C for 4 hours [121]. These alloys exhibited attractive magnetic properties: intrinsic coercivity ~ 17.7 kOe, maximum energy product $(\text{BH})_{\text{max}} \sim 12$ MGOe and Curie temperature $\sim 470^\circ\text{C}$. The secondary phases SmFe_2 and SmFe_3 were obtained during processing and $\text{Sm}_2\text{Fe}_{17}$ -nitride was subsequently fully decomposed into SmN and $\alpha\text{-Fe}$. The Sm-richer compositions are more recommended as Sm-poorer compositions are more prone to give $\alpha\text{-Fe}$, an undesirable phase.

Magnetically hard $\text{SmFe}_{7+x}\text{M}_x$ compounds were obtained by rapid solidification. Initially, the pure elements (99.9%) of Sm, Fe, and M (M = Mo, Ti, and V) were melted by induction heating to obtain the precursor $\text{SmFe}_{7+x}\text{M}_x$, which was subsequently melt spun at a linear velocity of 30 m/s followed by annealing at $650\text{--}750^\circ\text{C}$ in an inert atmosphere [122]. The hardness was attributed to the crystalline $\text{Sm}(\text{Fe},\text{M})_7$ phase, which exhibited high Curie temperature $\sim 355^\circ\text{C}$ with a high intrinsic coercivity of $\sim 3\text{--}7$ kOe, high remanence of 8 kG, and the maximum energy product of 5 MGOe. The high Curie temperature value was attributed to the extended solid solubility of

the additives (transition elements) in the $\text{Sm}(\text{Fe},\text{M})_7$ cells causing ~4.7%–6.7% volume expansion.

SmFeN magnets (isotropic as well as anisotropic) can be produced by three routes: mechanical alloying, HDDR, and Zn-bonded technique. SmFeN magnets obtained by mechanical alloying showed much higher coercivity compared to the same obtained by Zn-bonded magnets. The higher coercivity obtained in the former case can be attributed to the single-domain particles obtained through mechanical alloying compared to the multi-domain structure obtained in the latter case [123].

The addition of tungsten in SmFeN- α -Fe nanocomposite magnets influences both the microstructure and the magnetic properties (intrinsic properties) (of the Sm-Fe-N phase). A series of Sm-Fe-W alloys were produced by high-energy ball milling using elemental powders in Ar atmosphere (balls-to-powder ratio was 5). After milling, the powders were annealed at a temperature of 620°C for 1 hour in a vacuum of 10^{-3} Pa followed by nitriding carried out at 460°C for 1 hour [124].

Tungsten dissolves in the $\text{Sm}_2\text{Fe}_{17}\text{N}_3$ phase but does not dissolve in α -Fe. Some reduction of α -Fe grain size is observed in samples containing W, whereas the grain size of the $\text{Sm}_2(\text{Fe},\text{W})_{17}\text{N}_3$ phase remains constant. Tungsten exists in the microstructure in the form of small regularly dispersed grains. The remanence decreases for higher W contents but up to 10 at.% W is still enhanced. As the effect of these changes, the $(\text{BH})_{\text{max}}$ value achieves its maximum of 120 kJ/m³ for 2% W. The decrease in the remanence for doped magnets results from the existence of inclusions of a nonferromagnetic phase (W) and for higher W contents, the formation of W/ $\text{Sm}_2\text{Fe}_{17}\text{N}_3$ boundaries, which lower the effect of remanence enhancement.

The addition of alloying elements changes the microstructure and magnetic properties of the SmFeN magnets significantly [125–128]. The main key to get success in this process is to achieve α -Fe-free $\text{Sm}_2\text{Fe}_{17}$ due to the stabilization of the TFe₂ Laves phases, where T is Ti, Nb, Zr, Ta, Hf, and V. A technique has been mentioned to produce α -Fe-free $\text{Sm}_2\text{Fe}_{17}$ by adding 4%–5% Nb in the melt and a subsequent nitriding procedure of the material in the presence of N₂ to produce $\text{Sm}_2\text{Fe}_{17}\text{N}$ [125]. In this case, the soft α -Fe phase was replaced by the paramagnetic NbFe₂ phase. For the unbounded powder, the coercivity was observed at 0.2 T for the alloy with 5% Nb addition, and this material was highly comparable to the alloy obtained by long annealing at 1000°C. And eventually, this process was able to develop the efficient processing routes for the nitrogenated powder.

Since the discovery in 1990, SmFeN is considered as a potential candidate for use as a high-energy permanent magnet due to its excellent magnetic properties. At a higher temperature (~500°C), SmFeN dissociates into α -Fe and SmN, where α -Fe is a soft phase and deteriorates the magnetic properties. As a result, the application of this type of magnet is limited to

as bonded magnets. $\text{Sm}_2\text{Fe}_{17}$ phase is formed through a peritectic reaction where some $\alpha\text{-Fe}$ forms ($\sim 25\%$ of the phases present). The formation of this detrimental $\alpha\text{-Fe}$ phase can be avoided/removed by extended vacuum or inert atmosphere heat treatment, which is not only expensive but also detrimental to the environment and difficult to maintain the precise composition due to Sm evaporation. Earlier research showed that the addition of third elements, such as Nb, Zr, and Ta, can reduce the formation of primary $\alpha\text{-Fe}$ to a large extent.

Ta addition in SmFeN improved the microstructure and magnetic properties (coercivity) significantly. Alloys of $\text{Sm}_{13.8}\text{Fe}_{82.2}\text{Ta}_{4.0}$ and binary SmFe were prepared using HDDR process and were subsequently nitrided/nitrogenated to obtain SmFeTaN and SmFeN alloys [128]. Partly, the alloys were milled using attritor milling prior to the HDDR process. In the case of HDDR-processed samples, higher coercivity was obtained in the Ta-containing sample due to the presence of soft magnetic phase $\alpha\text{-Fe}$, which was replaced by TaFe_2 phase. Also, the coercivity of the pre-milled sample (sample attritor milled before HDDR) was higher because of the small particle size, produced by attritor milling prior to the HDDR process, which physically prevents the growth of large grains. **Table 7** shows the coercivity values and grain size obtained in both the cases.

The same research group found some different phase formations during Ta addition in SmFe binary alloy using HDDR process [129]: Ta_3Fe_7 along with $\text{Sm}_2\text{Fe}_{17}$, SmFe_2 , and SmFe_3 phases. In the case of Ta-containing alloy, dissolution of 2.0% of Ta into the 2:17 phase increased its stability with respect to decomposition in a hydrogen atmosphere. Initially, Ta was dissolved in the $\text{Sm}_2(\text{Fe,Ta})_{17}$ phase in the cast structure; however, in the HDDR process, Ta-based precipitates were formed leaving the 2:17 phase with 1.2% dissolved Ta.

Zr addition (1 at.%) in the SmFe alloy can avoid the formation of soft magnetic phase $\alpha\text{-Fe}$ [127]. Without going for any time-consuming homogenization process, the nonhomogenized $\text{Sm}_{10.5}\text{Fe}_{88.5}\text{Zr}_{1.0}$ alloy was able to achieve the coercivity as high as 3.1 T and the maximum energy product $(\text{BH})_{\text{max}} \sim 136 \text{ kJ/m}_3$. The nonhomogenized $\text{Sm}_{10.5}\text{Fe}_{88.5}\text{Zr}_{1.0}$ was milled and annealed at vacuum and subsequently nitrogenated, resulting in

Table 7. Coercivity and Grain Size Obtained in HDDR-Processed Material and Pre-Attritor Milled Material

| Type of Processing | Coercivity (kA/m) | | Grain Size (μm) |
|------------------------------|-------------------|---------|------------------------------|
| | SmFeN | SmFeTaN | |
| HDDR-processed material | 360 | 680 | ~ 100 |
| Pre-attritor milled material | 1010 | 1280 | ~ 5 |

anisotropic magnetic powders having coercivity of ~ 2.0 T and energy product $(BH)_{\max}$ of ~ 136 kJ/m³, whereas the HDDR treatment and subsequent nitro-generation resulted in isotropic magnetic powder having coercivity as high as 3.1 T and energy product $(BH)_{\max} \sim 103$ kJ/m³.

Injection-molded Sm–Fe–N magnets exhibited improved magnetic properties [130]. Yamamoto combined Nd–Fe–B powders with Sm–Fe–N powders to obtain an excellent energy product $(BH)_{\max}$ over 160 kJ/m³.

Although several attempts have been made to develop the interstitially modified magnets, still they are thermodynamically unstable at high temperature, which prevents them to be used as high-temperature magnets.

3.4 New materials/nanocomposites/thin-film magnets

Recently, in the nanotechnology era, developments in the microelectromechanical system (MEMS) technology and nanoelectromechanical system (NEMS) technology have stimulated the research activity on rare-earth-based permanent magnet thin films. Whether the film is rapidly solidified or not depends on the film deposition parameters (deposition temperature/substrate temperature, deposition time, rate of deposition, and substrate temperature), the substrate material (their heat-transfer coefficient), and the film deposition technology/method (sputtering, pulsed laser deposition, high-rate sputtering).

Jiang et al. reported an improved permanent magnet (hard ferromagnets) produced by deposition of multilayers of nanometer-thick Sm–Co and Fe, which behave as a nanocomposite [131]. Here, the energy product $(BH)_{\max}$ of the nanocomposite hard magnets depends on the film thickness of the multilayered magnets. For a specific Sm–Co layer thickness, as the thickness of the Fe layer decreases in the nanocomposite magnet, the $(BH)_{\max}$ of the film increases in the multilayered film.

Fabrication of $[\text{Sm}(\text{Co,Cu})_5/\text{Fe}]_6$ multilayer film was reported with in-plane texture and a high maximum energy product $(BH)_{\max}$ of 256 kJ/m³, which is larger than the theoretical limit of $(BH)_{\max}$ for SmCo_5 . The improved magnetic properties can be attributed to strong exchange coupling between the $\text{Sm}(\text{Co,Cu})_5$ and Fe layers, which was clearly understood from the single-phase behavior and the irreversible rotation in the demagnetization process [132]. Uehara et al. reported a multilayered structure made of Co-free/Co-doped Nd–Fe–B film layer (~ 200 nm) with Ta layer (~ 10 nm), which showed better magnetic property (enhanced energy product) compared to the monolayered Nd–Fe–B film magnets [133]. The multilayered film was sputtered on a heated glass substrate. The higher energy product achieved in the multilayered film can be attributed to the formation of the highly textured (perpendicular alignment) $\text{Nd}_2\text{Fe}_{14}\text{B}$ phase having small sized grains (size was controlled by the thickness of the unit layer). This perpendicularly

anisotropic multilayered magnetic film exhibited the magnetic properties of $H_{cJ} = 979$ kA/m, $J_r = 1.44$ T, and $(BH)_{\max} = 364$ kJ/m³. Recently, high-performance hard magnetic Nd–Fe–B-sputtered films were developed using high-rate sputtering onto 100 mm Si substrates [134]. The thickness of the film was ~ 5 μm and was deposited at 500°C. With a columnar grain structure, the film showed much improved magnetic properties of $H_{cJ} = 1.28$ MA/m and $(BH)_{\max} = 400$ kJ/m³. The coercivity was improved as high as 2.08 MA/m by varying (increasing) the Nd content in the films [135]. The increase in coercivity (enhanced coercivity up to $H_{cJ} = 2.08$ MA/m) was also reported by another group. Oka et al. [136] reported enhanced coercivity by the deposition of Cu layer on Nd–Fe–B thin-film layers. Sato et al. [137] reported a further enhancement of coercivity up to 2.50 MA/m by depositing of Nd–Cu layered structure. Thick-film magnets are ideal to use in magnetic microactuators. Nd–Fe–B thick-film magnets (thickness > 10 μm) were fabricated by high-speed pulsed laser deposition and obtained good magnetic properties of $(BH)_{\max} = 120$ kJ/m³ [138].

4 Applications of rare-earth permanent magnets

The rare-earth-based permanent magnets have a wide range of applications starting from the mobile phone and refrigerator in our daily life to modern science and technology such as MRI and other innovative systems. Some of those applications are discussed below. The important applications of the rare-earth-based permanent magnets can be mainly categorized as [23]

1. *Computer peripheral*: Disk drive spindle motors and voice coil motors, CD-ROM spindle motors, pick-up motors
2. *Office automation*: Printer and fax stepper motors, printer hammer, copy machine rollers
3. *Consumer electronics*: VCRs and camcorders, cameras, speakers (acoustic applications), headsets, microphones, pagers, DVD players, watches, cell phones
4. *Automotive*: Starter motors, electric steering, sensors, electric fuel pumps, motors in hybrid cars, instrumentation gauges, brushless DC motors, actuators, alternators
5. *Acoustic application*: Speaker (loud speakers)
6. *Appliances*: Portable power tools, household appliance motors, scales, air conditioners, water pumps, security systems
7. *Factory automation*: Magnetic couplings, pumps, motors, servo motors, generators, bearings
8. *Medical*: MRI, surgical tools, implants, "therapeutic"

Figure 27 shows the areas of the most important applications of the permanent magnets according to their sales distributions [139]. According to Figure 27, the largest application is in motors and generators. The second largest area of application is the acoustic devices (loudspeakers, headphones, microphones) and the measuring and control devices (NMR tomography). A substantial number of permanent magnets are used in telecommunications and data storage technology (computer peripheral, printers) and in magnetomechanical applications (couplings, bearings).

Figure 28 explains the extent of use of different permanent magnets. The most widely used ferrites occupy about 55% of the worldwide market for permanent magnets followed by the Nd–Fe–B and the Sm–Co magnets. The rare-earth magnets occupy about 37% of the world market and most of the remainder is Alnico [140]. Ferrites are used when the cost factor is very important, the Nd–Fe–B magnets are used when the size factor is important, and the Sm–Co magnets are used when the high-temperature stability is required [139].

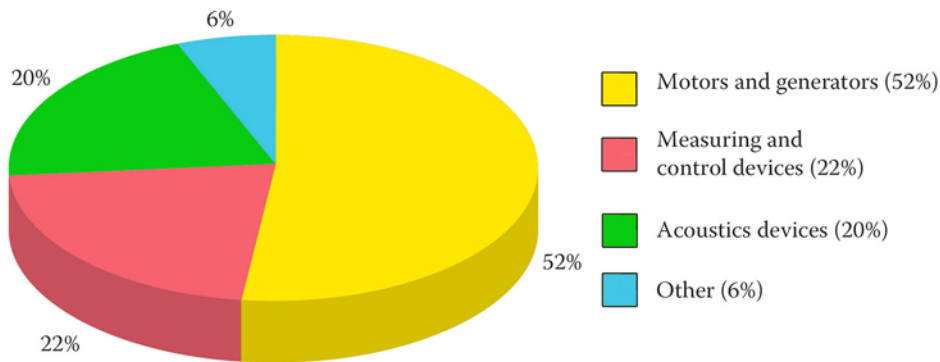


Figure 27. Use of rare-earth permanent magnets in different sectors.

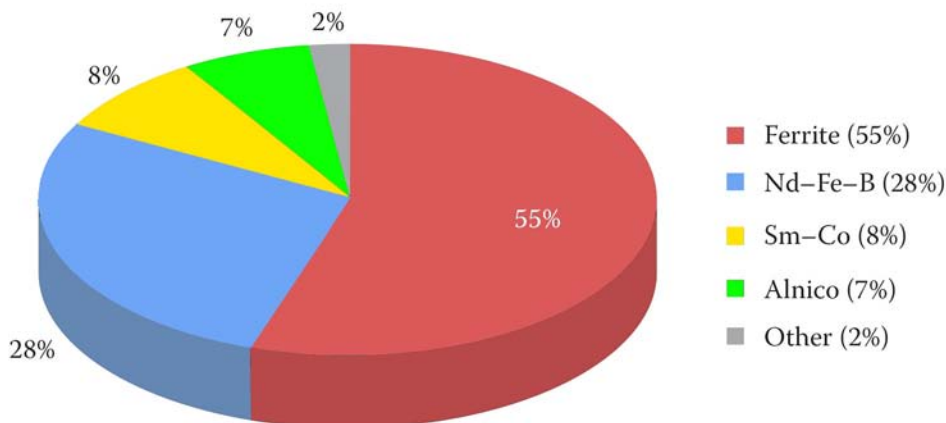


Figure 28. Estimated worldwide market for permanent magnet materials.

Literature says that according to the recent trends of selling market, output of the bonded magnets has enormously increased in China showing the huge increase in share with the growth rate of over 110% each year [141,142], whereas Japan shows a significant decrease in its share in the worldwide share market of rare-earth-bonded magnets, although the output of ferrite-bonded magnets is much higher compared to the same of rare-earth-bonded magnets in Japan.

A major application area for Nd-Fe-B magnets is the data storage industry [143]. Spindle motors hard disk drives utilize bonded Nd-Fe-B magnets, while sintered $\text{Nd}_2\text{Fe}_{14}\text{B}$ magnets are used in CD-lens actuators and voice coil motors (VCM), which are the actuator of the arm of HDD read/write heads. Another growing area for Nd-Fe-B magnets is electric motor and related applications [23]. A huge expansion area for the Nd-Fe-B magnets is the mobile phone where Nd-Fe-B magnets are used in the isolators of the microwave stations [23]. About 4% of Nd-Fe-B magnets are used in loudspeakers (thinner loudspeakers in car doors and outside ring layout in TVs and monitors) [143]. They are used in MRIs and automobiles as well. More widespread applications are considered in washing machines, refrigerators, and so on to improve energy efficiency and energy conservation [23]. The greatest potential markets are in the automobile industry where weight reduction, safe operation, and comfort improvements are required. To be used in HEVs (hybrid electric vehicles), the Nd-Fe-B magnets need high-temperature stability, which is difficult to achieve due to its low Curie temperature and high-temperature dependence of coercivity. To meet this requirement (high heat resistance) recently, the Nd-Fe-B magnets contains a large amount of Dy [30].

Sm-Co-based alloys are useful especially for high-temperature applications (sometimes as high as $\sim 500^\circ\text{C}$) in the fields of space, aeronautics, and electric vehicles [89]. SmCo_5 - and $\text{Sm}_2\text{Co}_{17}$ -type magnets have high magnetocrystalline anisotropies and high Curie temperatures over a wide temperature ranging from 50°C to 250°C . Also, these magnets exhibit high corrosion resistance. This high-temperature property and anticorrosive nature made them ideal for those applications where high-energy density magnets are needed and the magnetic field is stable over various environmental conditions with a wide range of temperature. Magnetic bearings, sensors and actuators, microwave tubes, gyroscopes and accelerometers, and reaction and momentum wheels to control and stabilize satellites are examples for those types of applications [3,4,144,145]. However, costly ingredients and difficulty in magnetization limit the applications of these magnets.

Sm-Fe-N and other interstitial bonded magnets are used for small motors.

5 Conclusions and future perspectives

Rare-earth magnets play an important role as essential functional parts in many devices, such as motors, relays, sensors, actuators, encoders, and valves. Rare-earth permanent magnets have become the key materials for the development of a sustainable future because they are now used in many applications, contributing to energy saving and greenhouse-gas reduction. In this chapter, we discussed the various processing routes of rare-earth permanent magnets based on rapid solidification techniques. The highest cooling rate obtained in these processes was about 10^9 – 10^{10} K/s and are usually used for laser-surface melting/remelting. For the production of rare-earth permanent magnets, the most favorable rapid solidification techniques are atomization and melt spinning where the microstructure scale and morphology can be monitored by controlling the process parameters and processing media to achieve desired magnetic properties for specific applications. Recently, some newly developed nanocomposites and thin-film magnets are able to accept the challenge to be used as the high-performance magnets (because of their high-energy products) in the MEMS or NEMS industry.

However, future studies and investigations on finding and developing new permanent magnet materials are strongly in demand—rare-earth-free permanent magnets.

For the high-temperature permanent magnetic materials, a new research direction may be the rare-earth-free magnetic materials that do not rely on the limited supply of the rare-earth metals and cost less. Further research is needed to bring the new rare-earth-free magnetic materials for high-temperature applications, and computational methods of combinational materials science may be helpful for the progress. Another area to explore is the interstitially modified rare-earth magnets, which are still under development. A major problem is their thermodynamic instability at high temperatures, which hampers application of these materials in fully dense sintered magnets.

Acknowledgments — The authors acknowledge the University of Nebraska-Lincoln, United States, and the Indian Institute of Technology, India, for their financial support throughout the study.

References

1. B. D. Cullity, *Introduction to Magnetic Materials*, Addison-Wesley Publishing Company, Reading, MA, 1972, p. 1.

2. J. M. D. Coey, in *Proceedings of the 14th International Workshop on Rare-Earth Magnets and Their Applications*, F. P. Missell, V. Villas-Boas, H. R. Rechenberg, and F. J. G. Landgraf (eds.), Sao Paulo, Brazil, 1996, Vol. 1, p. 1.
3. K. Strnat, G. Hoffer, J. Olson, W. Ostertag, and J. J. Becker, A family of new cobalt-base permanent magnet materials, *J. Appl. Phys.* 38, 1967, 1001.
4. K. J. Strnat, Rare earth-cobalt permanent magnets, in *Ferromagnetic Materials*, E. P. Wohlfarth and K. H. J. Buschow (eds.), Elsevier, Amsterdam, 1988, Vol. 4, pp. 131–210, Chapter 2.
5. K. J. Strnat, Modern permanent magnets for applications in electro-technology, *Proc. IEEE* 78, 1990, 923.
6. R. A. McCurrie, *Ferromagnetic Materials—Structure and Properties*, Academic Press Limited, San Diego, CA, 1994, p. 193.
7. O. Gutfleisch, Controlling the properties of high energy density permanent magnetic materials by different processing routes, *J. Phys. D Appl. Phys.* 33, 2000, R157–R172.
8. G. C. Hadjipanayis, J.-F. Liu, A. Gabay, and M. Marinescu, Current status in rare-earth permanent magnet research in USA, *J. Iron Steel Res. Int.* 13, 2006, 12–22.
9. J. J. Croat, J. F. Herbst, R. W. Lee, and F. E. Pinkerton, Pr-Fe and Nd-Fe-based materials: A new class of high-performance permanent magnets, *J. Appl. Phys.* 55, 1984, 2078.
10. J. J. Croat, J. F. Herbst, R. W. Lee, and F. E. Pinkerton, High-energy product Nd-Fe-B permanent magnets, *Appl. Phys. Lett.* 44, 1984, 148.
11. M. Sagawa, S. Fujimura, N. Togawa, H. Yamamoto, and Y. Matsuura, New material for permanent magnets on a base of Nd and Fe, *J. Appl. Phys.* 55, 1984, 2083.
12. S. J. Collocott, R. K. Day, and J. B. Dunlop, in *Proceedings of 7th International Symposium on Magnetic Anisotropy and Coercivity in Rare-Earth Transition Metal Alloys (Canberra, Australia)*, Hi-Perm Laboratory, Research Center for Advanced Mineral and Materials Processing, The University of Western Australia (ed.), Scott Four Colour Print, Perth, 1992, pp. 437–444.
13. J. M. Cadogan, H. S. Li, A. Margarian, J. B. Dunlop, D. H. Ryan, S. J. Collocott, and R. L. Davis, New rare-earth intermetallic phases $R_3(Fe, M)_{29}X_n$: (R = Ce, Pr, Nd, Sm, Gd; M = Ti, V, Cr, Mn; and X = H, N, C), *J. Appl. Phys.* 76, 1994, 6138.
14. K. Kobayashi, Some aspects of the present status of Sm_2Fe_{17} nitrides, in *Proceedings of 13th International Workshop on REM and Their Applications (Birmingham, UK)*, C. A. F. Manwaring, D. G. R. Jones, A. J. Williams, and I. R. Harris (eds.), The University of Birmingham, Birmingham, 1994, pp. 717–732.
15. H. Fujii and H. Sun, Interstitially modified intermetallics of rare earth and 3D elements, in *Handbook of Magnetic Materials*, K. H. J. Buschow (ed.), Elsevier, Amsterdam, 1995, Vol. 9, pp. 303–404, Chapter 3.
16. J. M. D. Coey, Permanent magnet applications—Topical review. *J. Magn. Magn. Mater.* 248, 2002, 441–456.
17. S. Aich, Crystal structure, microstructure and magnetic properties of SmCo-based permanent magnets, PhD dissertation, University of Nebraska, Lincoln, NE, 2005.

18. R. A. McCurrie, *Ferromagnetic Materials—Structure and Properties*, Academic Press Limited, San Diego, CA, 1994, p. 255.
19. T. Ojima, S. Tomizawa, T. Yoniyama, and T. Hori, Magnetic properties of a new type of rare-earth cobalt magnets $\text{Sm}_2(\text{Co}, \text{Cu}, \text{Fe}, \text{M})_{17}$, *IEEE Trans. Magn.* 13, 1977, 1317.
20. D. Li, H. F. Mildrum, and K. J. Strnat, Thermal stability of five sintered rare-earth–cobalt magnet types. *J. Appl. Phys.* 63, 1988, 3984.
21. T. Sun, A model on the coercivity of the hardened 2–17 rare earth-cobalt permanent magnets, *J. Appl. Phys.* 52, 1981, 2532.
22. J. F. Liu, Y. Zhang, D. Dimitar, and G. C. Hadjipanayis, Microstructure and high temperature magnetic properties of $\text{Sm}(\text{Co}, \text{Cu}, \text{Fe}, \text{Zr})_z$ ($z = 6.7\text{--}9.1$) permanent magnets, *J. Appl. Phys.* 85, 1999, 2800.
23. D. Brown, B.-M. Ma, and Z. Chen, Developments in the processing and properties of NdFeb-type permanent magnets, *J. Magn. Magn. Mater.* 248, 2002, 432–440.
24. J. Fidler, S. Sasaki, and E. Estevez-Rams, High performance magnets—Microstructure and coercivity, in *Material Research Society Symposium Proceedings on Advanced Hard and Soft Magnets*, MRS Proceedings, Cambridge University Press, 1999, Vol. 577, p. 291.
25. M. Endoh and M. Shindo, Material design and fabrication of high energy Nd–Fe–B sintered magnets, in *Proceedings of 13th International Workshop on RE Magnets and Their Applications*, C. A. F. Manwaring et al. (eds.), Birmingham, UK, 1994, Vol. 1, p. 397.
26. W. Rodewald, B. Wall, and W. Fernengel, Grain growth kinetics in sintered Nd–Fe–B magnets, *IEEE Trans. Magn.* 33, 1997, 3841.
27. O. Gutfleisch, A. Bollero, A. Handstein, D. Hinz, A. Kirchner, A. Yan, K.-H. Müller, and L. Schultz, Nanocrystalline high performance permanent magnets, *J. Magn. Magn. Mater.* 242–245, 2002, 1277–1283.
28. O. Gutfleisch, A. Teresiak, B. Gebel, K.-H. Müller, N. B. Cannesan, D. N. Brown, and I. R. Harris, Metastable borides and the inducement of texture in $\text{Pr}_2\text{Fe}_{14}\text{B}$ -type magnets produced by HDDR, *IEEE Trans. Magn.* 37, 2001, 2471.
29. R. N. Faria, A. J. Williams, and I. R. Harris, High anisotropy in Pr–Fe–Co–B–Zr HDDR powders, *J. Alloys Compd.* 287, 1999, L10.
30. S. Sugimoto, Current status and recent topics of rare-earth permanent magnets, *J. Phys. D Appl. Phys.* 44, 2011, 064001.
31. L. Cao, K. H. Muller, A. Handstein, W. Grunberger, and L. Neu Vand Schultz, High performance permanent magnets made by mechanical alloying and hot pressing, *J. Phys. D Appl. Phys.* 29, 1996, 271.
32. G. K. Williamson and W. H. Hall, X-ray line broadening from filed aluminium and wolfram, *Acta Metall.* 1, 1953, 22.
33. O. Gutfleisch, M. Matzinger, J. Fidler, and I. R. Harris, Characterisation of solid-HDDR processed $\text{Nd}_{16}\text{Fe}_{76}\text{B}_8$ alloys by means of electron microscopy, *J. Magn. Magn. Mater.* 147, 1995, 320.
34. M. Okada, K. Saito, H. Nakamura, S. Sugimoto, and M. Homma, Microstructural evolutions during HDDR phenomena in $\text{Sm}_2\text{Fe}_{17}\text{N}_x$ compounds, *J. Alloys Compd.* 231, 1995, 60.

35. O. Gutfleisch, M. Kubis, A. Handstein, K.-H. Muller, and L. Schultz, Hydrogenation disproportionation desorption recombination in Sm–Co alloys by means of reactive milling, *Appl. Phys. Lett.* 73, 1998, 3001.
36. A. Bollero, M. Kubis, O. Gutfleisch, K. H. Muller, and L. Schultz, Hydrogen disproportionation by reactive milling and recombination of $\text{Nd}_2(\text{Fe}_{1-x}\text{Co}_x)_{14}\text{B}$ alloys, *Acta Mat.* 48, 2000, 4929–4934.
37. X. L. Yeh, K. Samwer, and W. L. Johnson, Formation of an amorphous metallic hydride by reaction of hydrogen with crystalline intermetallic compounds—A new method of synthesizing metallic glasses, *Appl. Phys. Lett.* 42, 1983, 242.
38. L. Schultz, K. Schnitzke, J. Wecker, M. Katter, and C. Kuhrt, Permanent magnets by mechanical alloying (invited), *J. Appl. Phys.* 70, 1991, 6339.
39. J. Ding, P. G. McCormick, and R. Street, A study of $\text{Sm}_{13}(\text{Co}_{1-x}\text{Fe}_x)_{87}$ prepared by mechanical alloying, *J. Magn. Magn. Mater.* 135, 1994, 200.
40. J. Ding, P. G. McCormick, and R. Street, Remanence enhancement in mechanically alloyed isotropic $\text{Sm}_7\text{Fe}_{93}$ -nitride, *J. Magn. Magn. Mater.* 124, 1993, 1.
41. K. Schnitzke, L. Schultz, J. Wecker, and M. Katter, High coercivity in $\text{Sm}_2\text{Fe}_{17}\text{N}_x$ magnets, *Appl. Phys. Lett.* 57, 1990, 2853.
42. J. Ding, B. Shen, P. G. McCormick, R. Street, and F. Wang, Magnetic hardening of mechanically milled $\text{Sm}_2\text{Fe}_{14}\text{Ga}_3\text{C}_2$, *J. Alloys Compd.* 209, 1994, 221.
43. Y. Yang, O. Gutfleisch, A. Handstein, D. Eckert, and K. H. Muller, High coercivity of Nd–Dy–Fe–(C, B) ribbons prepared by melt spinning, *Appl. Phys. Lett.* 76, 2000, 3627.
44. P. Crespo, V. Neu, and L. Schultz, Mechanically alloyed nanocomposite powders of $\text{Nd}_2\text{Fe}_{14}\text{B}/\alpha\text{-Fe}$ with additional elements, *J. Phys. D Appl. Phys.* 30, 1997, 2298.
45. Z. Chen, X. Meng-Burany, and G. C. Hadjipanayis, High coercivity in nanostructured PrCo_5 -based powders produced by mechanical milling and subsequent annealing, *Appl. Phys. Lett.* 75, 1999, 3165.
46. Shi Gang, Hu Lianxi, and Wang Erde, Preparation, microstructure, and magnetic properties of a nanocrystalline $\text{Nd}_{12}\text{Fe}_{82}\text{B}_6$ alloy by HDDR combined with mechanical milling, *J. Magn. Magn. Mat.* 301, 2006, 319–324.
47. R. M. German, *Powder Metallurgy Science*, 2nd ed., Metal Powder Industries Federation (MPIF), Princeton, NJ, 1994, ISBN-13: 978-1878954428.
48. W. M. Steen, *Laser Material Processing*, Springer Verlag, New York, 1991.
49. J. E. Gusic, H. W. Marcos, and L. G. von Uiter, Laser oscillations in Nd-doped yttrium aluminum, yttrium gallium and gadolinium garnets, *App. Phys. Lett.* 4, 1964, 182.
50. C. K. N. Patel, Continuous-wave laser action on vibrational-rotational transitions of CO_2 , *Phys. Rev.* 136A, 1964, 1187.
51. J. Laeng, J. C. Stewart, and F. W. Liou, Laser metal forming processes for rapid prototyping—A review, *Int. J. Prod. Res.* 38, 2000, 3973–3996.
52. W. Wiehua-Wang, M. R. Holl, and D. T. Schwartz, Rapid prototyping of masks for through-mask electrodeposition of thick metallic components, *J. Electrochem. Soc.* 148, 2001, C363–C368.

53. A. Greco, A. Licciulli, and A. Maffezzoli, Stereolithography of ceramic suspensions, *J. Mater. Sci.* 36, 2001, 99–105.
54. L. Lu, J. Y. H. Fuh, Z. D. Chen, C. C. Leong, and Y. S. Wong, In situ formation of TiC composite using selective laser melting, *Mater. Res. Bull.* 35, 2000, 1555–1561.
55. K. Daneshvar, M. Raissi, and S. M. Bobbio, Laser rapid prototyping in nonlinear medium, *J. Appl. Phys.* 88, 2000, 2205–2210.
56. J. P. Kruth, M. Badrossamay, E. Yasa, J. Deckers, L. Thijs, and J. van Humbeeck, Part and material properties in selective laser melting of metals, in *Proceedings of the 16th International Symposium on Electro-Machining*, 2010, Wansheng Zhao et al. (eds.), Shanghai Jiao Tong University Press, Shanghai.
57. https://en.wikipedia.org/wiki/Electrospinning#/media/File:Electrospinning_Image_for_Wikipedia.tif
58. R. W. Cahn, Background to rapid solidification processing, in *Rapidly Solidified Alloys*, H. H. Liebermann (ed.), Marcel Dekker, New York, 1993, p. 1.
59. T. R. Anantharaman and C. Suryanarayana, *Rapidly Solidified Metals*, Trans Tech Publications, Switzerland, 1987, p. 25.
60. C. Suryanarayana, Rapid solidification, in *Processing of Metals and Alloys*, R. W. Cahn (ed.), Trans Tech Publications, Switzerland, 1991, p. 57.
61. N. J. Grant, H. Jones, and E. J. Lavernia, Synthesis and processing, in *Elements of Rapid Solidification—Fundamentals and Applications*, M. A. Otonari (ed.), Springer, 1998, p. 35, ISBN 978-3-642-45755-5.
62. J. O. Strom-Olsen, Fine fibers by melt extraction, *Mater. Sci. Eng. A* 178, 1994, 239–243.
63. G. Hoffer and K. J. Strnat, Magnetocrystalline anisotropy of YCo_5 and Y_2Co_{17} , *IEEE Trans. Magn. Magn.* 2, 1966, 487.
64. A. E. Ray and K. J. Strnat, Research and development of rare earth-transition metal alloys as permanent-magnet materials, Technical Report AFML-TR-72-99, 1972.
65. H. Saito, M. Takahashi, T. Wakiyama, G. Kodo, and H. Nakagawa, Magnetocrystalline anisotropy for $\text{Sm}_2(\text{Co-Mn})_{17}$ compound with TbCu_7 type disordered structure, *J. Magn. Magn. Mater.* 82, 1989, 322.
66. K. H. Buschow and F. J. A. den Breder, The cobalt-rich regions of the samarium-cobalt and gadolinium-cobalt phase diagrams, *J. Less-Common Met.* 3, 1973, 191.
67. M. Q. Huang, W. E. Wallace, M. McHenry, Q. Chen, and B. M. Ma, Structure and magnetic properties of $\text{SmCo}_{7-x}\text{Zr}_x$ alloys ($x = 0-0.8$), *J. Appl. Phys.* 83, 1998, 6718.
68. M. Q. Huang, M. Drennan, W. E. Wallace, M. E. McHenry, Q. Chen, and B. M. Ma, Structure and magnetic properties of $\text{RCo}_{7-x}\text{Zr}_x$ ($R = \text{Pr or Er}$, $x = 0-0.8$), *J. Appl. Phys.* 85, 1999, 5663.
69. J. Zhou, I. A. Al-Omari, J. P. Liu, and D. J. Sellmyer, Structure and magnetic properties of $\text{SmCo}_{7-x}\text{Ti}_x$ with TbCu_7 -type structure, *J. Appl. Phys.* 87, 2000, 5299.

70. S. Aich and J. E. Shield, Phase formation and magnetic properties of SmCo_{5+x} alloys with TbCu_7 -type structure, *J. Magn. Magn. Mater.* 279, 2004, 76–81.
71. K. H. J. Buschow and A. S. van der Goot, Composition and crystal structure of hexagonal Cu-rich rare earth–copper compounds, *Acta Cryst. Allogr. B* 27, 1971, 1085.
72. I. A. Al-Omari, Y. Yeshurun, J. Zhou, and D. J. Sellmyer, Magnetic and structural properties of $\text{SmCo}_{7-x}\text{Cu}_x$ alloys, *J. Appl. Phys.* 87, 2000, 6710.
73. J. Luo, J. K. Liang, Y. Q. Guo, Q. L. Liu, L. T. Yang, F. S. Liu, G. H. Rao, and W. Li, Effects of Cu on crystallographic and magnetic properties of $\text{Sm}(\text{Co}, \text{Cu})_7$, *J. Phys. Condens. Matter* 15, 2003, 5621.
74. J. Luo, J. K. Liang, Y. Q. Guo, Q. L. Liu, F. S. Liu, Y. Zhang, L. T. Yang, and G. H. Rao, Effects of the doping element on crystal structure and magnetic properties of $\text{Sm}(\text{Co}, \text{M})_7$ compounds (M: Zr, Cu, Ti, Zr, and Hf), *Intermetallics* 13, 2005, 710–716.
75. Y. Q. Guo, W. Li, J. Luo, W. C. Feng, and J. K. Liang, Structure and magnetic characteristics of novel SmCo-based hard magnetic alloys, *J. Magn. Magn. Mater.* 303, 2006, 367–370.
76. A. R. Miedema, The heat of formation of alloys, *Philips Technol. Rev.* 36, 1976, 217.
77. A. R. Miedema, R. Boom, and F. R. De Boer, On the heat of formation of solid alloys, *J. Less-Common Met.* 41, 1975, 283.
78. A. K. Niessen, F. R. de Boer, R. Boom, P. F. De Chatel, M. C. M. Mattens, and A. R. Miedema, Model predictions for the enthalpy of formation of transition metal alloys II, *Calphad* 7, 1983, 51.
79. J. Luo, J. K. Liang, Y. Q. Guo, L. T. Yang, F. S. Liu, Y. Zhang, Q. L. Liu, and G. H. Rao, Crystal structure and magnetic properties of $\text{SmCo}_{7-x}\text{Hf}_x$ compounds, *Appl. Phys. Lett.* 85, 2004, 5299.
80. S. K. Chen, M. S. Chu, J. L. Tsai, and T. S. Chin, Magnetic properties of microcrystalline SmCo_x alloys by melt spinning, *IEEE Trans. Magn.* 32, 1996, 4419.
81. G. C. Hadjipanayis, Nanophase hard magnets, *J. Magn. Magn. Mater.* 200, 1999, 373.
82. W. Gong and B. M. Ma, Comparison on the magnetic and structural properties of $\text{Sm}(\text{Co}_{0.67-x}\text{Fe}_{0.25}\text{Cu}_{0.06}\text{Zr}_{0.02}\text{C}_x)_{8.0}$, where $x = 0-0.15$, melt spun ribbons and cast alloys, *J. Appl. Phys.* 85, 1999, 4657.
83. J.-B. Sun, D. Han, C.-X. Cui, W. Yang, L. Li, and F. Yang, Effects of quenching speed on microstructure and magnetic properties of novel $\text{SmCo}_{6.9}\text{Hf}_{0.1}(\text{CNTs})_{0.05}$ melt-spun ribbons, *Acta Mater.* 57, 2009, 2845–2850.
84. J.-B. Sun, D. Han, C.-X. Cui, W. Yang, H. Zhou, R.-T. Tian, and L.-G. Yang, Effect of Hf and CNTs on magnetic transformation and thermal stabilities of TbCu_7 -type Sm-Co matrix ribbon magnets, *J. Alloys Compd.* 487, 2009, 626–630.
85. J.-B. Sun, D. Han, C.-X. Cui, W. Yang, L. Li, F. Yang, and L.-G. Yang, Effects of Hf and CNTs on structure and magnetic properties of TbCu_7 -type Sm-Co magnets, *Intermetallics* 18, 2010, 599–605.

86. H. W. Chang, S. T. Huang, C. W. Chang, C. H. Chiu, W. C. Chang, A. C. Sun, and Y. D. Yao, Magnetic properties, phase evolution and microstructure of melt-spun $\text{SmCo}_{7-x}\text{Hf}_x\text{C}_y$ ($x = 0-0.5$; $y = 0-0.14$) ribbons, *J. Appl. Phys.* 101, 2007, 09K508.
87. H. W. Chang, S. T. Huang, C. W. Chang, C. H. Chiu, I. W. Chen, W. C. Chang, A. C. Sun, and Y. D. Yao, Comparison on the magnetic properties and phase evolution of melt-spun SmCo_7 ribbons with Zr and Hf substitution, *Scr. Mater.* 56, 2007, 1099–1102.
88. S. Aich and J. E. Shield, Effect of Nb and C additives on the microstructures and magnetic properties of rapidly solidified Sm-Co alloys, *J. Alloys Compd.* 425, 2006, 416–423.
89. C.-B. Jiang and S.-Z. An, Recent progress in high temperature permanent magnetic materials, *Rare Met.* 32, 2013, 431–440.
90. L. L. Liu and C. B. Jiang, The improved oxidation resistance of Si-doped SmCo_7 nanocrystalline magnet, *Appl. Phys. Lett.* 98, 2011, 252504.
91. L. L. Liu, T. Y. Jin, and C. B. Jiang, High-temperature oxidation resistance and magnetic properties of Si-doped $\text{Sm}_2\text{Co}_{17}$ -type magnets at 500°C, *J. Magn. Mater.* 324, 2012, 2310.
92. Q. Y. Wang, L. Zheng, S. Z. An, T. Zhang, and C. Jiang, Thermal stability of surface modified $\text{Sm}_2\text{Co}_{17}$ -type high temperature magnets, *J. Magn. Mater.* 331, 2013, 245.
93. C. H. Chen, M. Q. Huang, J. E. Foster, G. Monnette, J. Middleton, A. Higgins, and S. Liu, Effect of surface modification on mechanical properties and thermal stability of Sm-Co high temperature magnetic materials, *Surf. Coat. Technol.* 201, 2006, 3430.
94. W. M. Pragnell, H. E. Evans, and A. J. Williams, Oxidation protection of $\text{Sm}_2\text{Co}_{17}$ -based alloys, *J. Alloys Compd.* 517, 2012, 92.
95. K.-H. Muller, G. Krabbes, J. Fink, S. Größ, A. Kirchner, G. Fuchs, and L. Schultz, New permanent magnets, *J. Magn. Mater.* 226–230, 2001, 1370–1376.
96. B. M. Ma, J. W. Herchenroeder, B. Smith, M. Suda, D. N. Brown, and Z. Chen, Recent development in bonded NdFeB magnets, *J. Magn. Mater.* 239, 2002, 418–423.
97. A. P. Guimaraes, *Principles of Nanomagnetism*, Springer, Berlin, 2009, XII, 224pp, available in: <http://www.springer.com/978-3-642-01481-9>
98. D. Goll, M. Seeger, and H. Kronmüller, Magnetic and microstructural properties of nanocrystalline exchange coupled PrFeB permanent magnets, *J. Magn. Mater.* 185, 1998, 49.
99. H. A. Davies, C. L. Harland, J. I. Betancourt, and G. Menozza, Document praseodymium and neodymium-based nanocrystalline hard magnetic alloys, in *Material Research Society Symposium Proceedings on Advanced Hard and Soft Magnets*, MRS Proceedings, Cambridge University Press, 1999, Vol. 577, p. 27.
100. J. F. Herbst, $\text{R}_2\text{Fe}_{14}\text{B}$ materials: Intrinsic properties and technological aspects, *Rev. Mod. Phys.* 63, 1991, 819.
101. J. J. Croat, Manufacture of $\text{Nd}_2\text{Fe}_{14}\text{B}$ permanent magnets by rapid solidification, *J. Less-Common Met.* 148, 1989, 7–15.

102. Z. W. Liu, Y. Liu, P. K. Deheri, R. V. Ramanujan, and H. A. Davies, Improving permanent magnetic properties of rapidly solidified nanophase RE–TM–B alloys by compositional modification, *J. Magn. Magn. Mater.* 321, 2009, 2290–2295.
103. C. D. Fuerst and E. G. Brewer, High-remanence rapidly solidified N&Fe-B: Die-upset magnets (invited), *J. Appl. Phys.* 73, 1993, 5751–5756.
104. E. F. Kneller and R. Hawig, The exchange-spring magnet: A new material principle for permanent magnets, *IEEE Trans. Magn.* 27, 1991, 3588.
105. S. Hirose, Nd-Fe-B-based nanocomposite permanent magnets suitable for strip casting, in *Proceedings of 18th International Workshop on High Performance Magnets and Their Applications (Annecy, France)*, N. M. Dempsey and P. de Rango (eds.), CNRS, Grenoble, 2004, Vol. 2, pp. 655–666.
106. O. M. Bovda, V. O. Bovda, V. V. Chebotarev, I. E. Garkusha, S. O. Leonov, L. V. Onischenko, V. I. Tereshin, and O. S. Tortika, Effect of pulsed plasma treatment on structure and corrosion behavior of Sm-Co and Nd-Fe-B magnets, *J. Iron Steel Res. Int.* 13, 2006, 337–342.
107. P. K. Sokolowski, Processing and protection of rare earth permanent magnet particulate for bonded magnet application, MSc thesis, Iowa State University, 2007.
108. J. M. D. Coey and H. Sun, Improved magnetic properties by treatment of iron-based rare earth intermetallic compounds in ammonia, *J. Magn. Magn. Mater.* 87, 1990, 251.
109. K. H. J. Buschow, F. H. Feijen, and K. de Kort, Rare earth permanent magnets, *J. Magn. Magn. Mater.* 140–144, 1995, 9–12.
110. R. Coehoom, K. H. J. Buschow, M. W. Dirken, and R. C. Thiel, Valence-electron contributions to the electric-field gradient in hcp metals and at Gd nuclei in intermetallic compounds with the ThCr₂Si₂ structure, *Phys. Rev. B* 42, 1990, 4645.
111. M. W. Dirken, R. C. Thiel, R. Coehoom, T. H. Jacobs, and K. H. J. Buschow, ¹⁵⁵Gd Mössbauer effect study of Gd₂Fe₁₇N_x, *J. Magn. Magn. Mater.* 94, 1991, L15.
112. D. P. Middleton, F. M. Mulder, R. C. Thiel, and K. H. J. Buschow, ¹⁵⁵Gd Mössbauer effect studies and magnetic properties of GdFe_{12-x}Mo_x(N_y) compounds, *J. Magn. Magn. Mater.* 146, 1995, 123–128.
113. P. A. P. Wendhausen, B. Gebel, D. Eckert, and K. H. Müller, Effect of milling on the magnetic and microstructural properties of Sm₂Fe₁₇N_x permanent magnets, *J. Appl. Phys.* 75, 1994, 6018.
114. N. M. Dempsey, P. A. P. Wendhausen, B. Gebel, K. H. Müller, and J. M. D. Coey, in *Proceedings of 14th International Workshop on Rare Earth Magnets and Their Applications*, F. P. Missell (ed.), Sao Paulo, Brazil, 1996, p. 349.
115. B. G. Shen, L. S. Kong, F. W. Wang, and L. Cao, A novel hard magnetic material for sintering permanent magnets, *J. Appl. Phys.* 75, 1994, 6253.
116. B. G. Shen, F. W. Wang, L. S. Kong, L. Cao, and W. S. Zhan, Structure and magnetic properties of Sm₂Fe₁₄Ga₃C_x (x = 0–2.5) compounds prepared by arc melting, *Appl. Phys. Lett.* 63, 1993, 2288.

117. Z. H. Cheng, B. G. Shen, F. W. Wang et al., The formation and magnetic properties of $\text{Sm}_2\text{Fe}_{15}\text{Al}_2\text{C}_x$ ($x = 0-2.0$) compounds prepared by arc melting, *J. Phys. Condens. Matter* 6, 1994, 1185.
118. R. Skomski, S. Brennan, and S. Wirth, in *Interstitial Metallic Alloys*, F. Grandjean, G. J. Long, and K. H. J. Buschow (eds.), Kluwer, Dordrecht, 1995, NATO-ASI Series E, Vol. 281, Chapter 16.
119. K. H. Muller, L. Cao, N. M. Dempsey, and P. A. P. Wendhausen, $\text{Sm}_2\text{Fe}_{17}$ interstitial magnets (invited), *J. Appl. Phys.* 79, 1996, 5045.
120. M. Kubis, D. Eckert, B. Gebel, K.-H. Müller, and L. Schultz, Intrinsic magnetic properties of $\text{Sm}_2\text{Fe}_{17-x}\text{M}_x\text{N}_y/\text{C}_y$ ($M = \text{Al, Ga or Si}$), *J. Magn. Magn. Mater.* 217, 2000, 14-18.
121. C. N. Christodoulou and T. Takeshita, $\text{Sm}_2\text{Fe}_{17}$ -nitride-based permanent magnets produced by rapid solidification, *J. Alloys Compd.* 196, 1993, 161-164.
122. C. J. Yang, E. B. Park, and S. D. Choi, Magnetic hardening of rapidly solidified $\text{SmFe}_{7+x}\text{M}_x$ ($0.8 \leq x \leq 1.5$, $M = \text{Mo, V, Ti}$) compounds, *Mater. Lett.* 24, 1995, 347-354.
123. X. C. Kou, Coercivity of SmFeN permanent magnets produced by various techniques, *J. Alloys Compd.* 281, 1998, 41-45.
124. W. Kaszuwara, M. Leonowicz, and J. A. Kozubowski, The effect of tungsten addition on the magnetic properties and microstructure of SmFeN- α -Fe nanocomposite, *Mater. Lett.* 42, 2000, 383-386.
125. A. E. Platts, I. R. Harris, and J. M. D. Coey, Improvement in the cast structure of Sm(2) Fe(17) alloys by niobium additions, *J. Alloys Compd.* 185, 1992, 251.
126. B. Saje, A. E. Platts, S. Kobe Besenicar, I. R. Harris, and D. Kolar, Microstructure and magnetic properties of Sm-Fe-Ta based alloys, *IEEE Trans. Magn.* 30, 1994, 690.
127. B. Gebel, M. Kubis, and K. H. Müller, Permanent magnets prepared from $\text{Sm}_{10.5}\text{Fe}_{88.5}\text{Zr}_{1.0}\text{N}_y$ without homogenization, *J. Magn. Magn. Mater.* 174, 1997, L1-L4.
128. K. Žužek, P. J. McGuinness, and S. Kobe, Bonded Sm-Fe-(Ta)-N materials produced via attritor milling and HDDR, *J. Alloys Compd.* 289, 1999, 265-269.
129. K. Zuzek, G. Drazic, P. J. McGuinness, and S. Kobe, High coercivity powders based on Sm-Fe-Ta-N prepared by a novel technique, *Phys. Solid State* 44, 2002, 1540-1543.
130. M. Yamamoto, *BM News* (The Japan Association of Bonded Magnetic Materials [JABM]), 43, 2010, 72 (in Japanese).
131. J. Jiang, E. Fullerton, C. Sowers, I. Inomata, S. Bader, A. Shapiro, R. Shull, V. Gornakov, and V. Nikitenko, Spring magnet films, *IEEE Trans. Magn.* 35, 1999, 3229.
132. J. Zhang, Y. K. Takahashi, R. Gopalan, and K. Hono, $\text{Sm}(\text{Co,Cu})_5/\text{Fe}$ exchange spring multilayer films with high energy product $\text{Sm}(\text{Co,Cu})_5/\text{Fe}$ exchange spring multilayer films with high energy product, *Appl. Phys. Lett.* 86, 2005, 122509.

133. M. Uehara, N. Gennai, M. Fujiwara, and T. Tanaka, Improved perpendicular anisotropy and permanent magnet properties in Co-doped Nd-Fe-B films multilayered with Ta, *IEEE Trans. Magn.* 41, 2005, 3838.
134. N. M. Dempsey, A. Walther, F. May, D. Givord, K. Khlopkov, and O. Gutfleisch, High performance hard magnetic NdFeB thick films for integration into micro-electromechanical systems, *Appl. Phys. Lett.* 90, 2007, 092509.
135. N. M. Dempsey, Presentation in the *2nd International Symposium on Advanced Magnetic Materials and Applications (ISAMMA 2010)*, Sendai, Japan, 2010, AX-07
136. N. Oka, T. Sato, Y. Mishina, and T. Shima, Presentation in the *33rd Annual Conference on Magnetism in Japan*, Nagasaki, Japan, 2009, 12pE-4 (in Japanese).
137. T. Sato, T. Ohsuna, and Y. Kaneko, in *Digests of the 34th Annual Conference on Magnetism in Japan 2010 (Tsukuba, Japan)*, The Magnetic Society of Japan, Tokyo, 2010, p. 272.
138. M. Nakano, S. Sato, F. Yamashita, T. Honda, J. Yamasaki, K. Ishiyama, M. Itakura, J. Fidler, T. Yanai, and H. Fukunaga, Review of fabrication and characterization of Nd-Fe-B thick films for magnetic micromachines, *IEEE Trans. Magn.* 43, 2007, 2672.
139. K. H. J. Buschow, Permanent magnet materials based on 3d-rich ternary compounds, in *Ferromagnetic Materials*, E. P. Wohlfarth and K. H. J. Buschow (eds.), Elsevier, Amsterdam, 1988, Vol. 4, p. 1.
140. Z. Yao and C. B. Jiang, Structure and magnetic properties of $\text{SmCo}_x\text{Ti}_{0.4-1}:7$ ribbons, *J. Magn. Magn. Mater.* 320, 2008, 1073–1077.
141. N. Ishigaki and H. Yamamoto, *Magnet. Japan* 3, 2008, 525.
142. H. Arakawa, *BM NEWS* (The Japan Association of Bonded Magnetic Materials [JABM]), 42, 2009, 9 (in Japanese).
143. R. H. J. Fastenau and E. J. Van Loenen, Applications of rare earth permanent magnets (invited paper), *J. Magn. Magn. Mater.* 157–158, 1996, 1–6.
144. K. Kumar, RETM_5 and $\text{RE}_2\text{TM}_{17}$ permanent magnets development, *J. Appl. Phys.* 63, 1988, R13.
145. A. E. Ray and S. Liu, in *Proceedings of 12th International Workshop on RE Magnets and Their Applications*, F. P. Missel (ed.), Canberra, Australia, 1992, p. 552.